Journal of Civil Structural Health Monitoring
https://doi.org/10.1007/s13349-021-00476-x

ORIGINAL PAPER

Strain predictions at unmeasured locations of a substructure using sparse response-only vibration measurements

Sofia Puerto Tchemodanova[1] · Masoud Sanayei[1] · Babak Moaveni[1] · Konstantinos Tatsis[2] · Eleni Chatzi[2]

Received: 2 October 2020 / Revised: 9 February 2021 / Accepted: 4 March 2021

Abstract
Structural health monitoring of complex structures is often limited by restricted accessibility to locations of interest within the structure and availability of operational loads. In this work, a novel output-only virtual sensing scheme is proposed. This scheme involves the implementation of the modal expansion in an augmented Kalman filter. The performance of the proposed scheme is compared with two existing methods. Method 1 relies on a finite element model updating, batch data processing, and modal expansion (MUME) procedure. Method 2 employs a recursive sequential estimation algorithm, which feeds a substructure model of the instrumented system into an augmented Kalman filter (AKF). The new scheme referred to as Method 3 (ME-AKF), implements strain estimates generated via Modal Expansion into an AKF as virtual measurements. To demonstrate the applicability of the aforementioned methods, a rollercoaster connection was instrumented with accelerometers, strain rosettes, and an optical sensor. A comparison of estimated dynamic strain response at unmeasured locations using three alternative schemes is presented. Although acceleration measurements are used indirectly for model updating, the response-only methods presented in this research use only measurements from strain rosettes for strain history predictions and require no prior knowledge of input forces. Predicted strains using all methods are shown to sufficiently predict the measured strain time histories from a control location and lie within a 95% confidence interval calculated based on modal expansion equations. In addition, the proposed ME-AKF method shows improvement in strain predictions at unmeasured locations without the necessity of batch data processing. The proposed scheme shows high potential for real-time dynamic estimation of the strain and stress state of complex structures at unmeasured locations.

Keywords Rollercoaster structure · Nondestructive testing · Structural health monitoring · Model updating · Modal identification · Modal expansion · Output-only system identification · Dynamic substructuring · Augmented Kalman filter · Strain predictions

1 Introduction

Structural complexity has increased over the decades as new structural systems, materials, construction methods, and innovative designs emerge. As an example of a complex structural system, this work presents a rollercoaster structure. Innovations in rollercoaster designs aim to increase the speed of the train along the tracks by means of rapid changes in altitude and track orientations in an effort to enhance the rider's experience by intensifying the passenger's thrill [1]. Similarly, the design of traditional infrastructure, e.g. buildings and bridges, has been growing in complexity due to the ever-increasing load capacity and traffic resulting in challenging structural designs.

Safety standards of complex structures, such as bridges, rollercoasters, or wind turbine towers, require frequent

✉ Masoud Sanayei
masoud.sanayei@tufts.edu

Sofia Puerto Tchemodanova
sofia.puerto@tufts.edu

Babak Moaveni
babak.moaveni@tufts.edu

Konstantinos Tatsis
tatsis@ibk.baug.ethz.ch

Eleni Chatzi
chatzi@ibk.baug.ethz.ch

[1] Department of Civil and Environmental Engineering, Tufts University, Medford, MA 02155, USA

[2] Department of Civil, Environmental and Geomatic Engineering, ETH Zurich, Zürich, Switzerland

Published online: 24 June 2021

inspections for assessment of structural condition [2–4]. These inspections are often visual and are carried out by maintenance crews going over the length of the structure (bridge girders and decks, railway tracks, rollercoaster tracks, wind turbine towers, etc.). Safety of maintenance procedures is of paramount importance. The development of remote sensing technologies and procedures for the assessment of complex structural components is essential for the improvement of workplace safety while preserving structural integrity. Remote monitoring and dynamic prediction of the response of the structure to live loads can provide meaningful and rapid information for decision-making on preventative maintenance, asset management, and structural safety.

Virtual sensing techniques can be implemented for the estimation of strains or stresses at inaccessible locations or critical points, where isolated sensor readings can be affected by localized effects due to stress concentrations [5, 6]. Estimation of strain time histories at unmeasured locations can be achieved using sparse measurements and methods which operate in both batch and recursive schemes. The first category operates on batches of the obtained measurements and utilizes an established mapping between measured and virtually predicted locations, such as the one provided by modal expansion [7–9]. On the other hand, recursive schemes such as those relying on Bayesian-type filters [10–12], offer an online sequential estimation. When real-time estimation is not required, schemes relying on Bayesian filters can also operate on batch data using smoothing algorithms to refine estimations [13, 14].

The use of limited sets of measured batch sets of strain time histories combined with an updated model and a modal expansion method has been shown to provide accurate strain time histories at unmeasured locations in a simple cantilever beam [15]. Full-field dynamic stress–strain predictions using an updated analytical model and expansion procedures have proven to provide reliable results in wind turbine structures and under various measured loading conditions [16]. Pingle and Avitabile's research demonstrated the robustness of modal expansion procedure using displacement data. Although noise can cause estimation uncertainty in results obtained using these procedures, it has been shown that if enough participating modes are included in the process the estimation error is minimal [17]. A more recent study shows that the expansion of experimental mode shapes by a finite element model has the potential to reduce stress/strain estimation errors [18]. This finding was reached by comparing the results obtained from using mode shapes from a finite element model to the results obtained from using expanded experimental mode shapes. Prediction of reliable strain time histories is also highly influenced by the quality of the mathematical model employed to represent the structure under study. The quality of the mathematical models can be improved through model updating. Among the most common approaches for model updating of linear dynamic systems is the eigensystem realization algorithm (ERA) [19] when combined with the natural excitation technique (NExT) [20]. The combined use of these two methodologies, NExT-ERA has shown to be effective in identifying modal parameters of real-size complex structures [21–23]. Acceleration measurements are commonly used when employing modal identification algorithms. However, strain measurements have been found to be as informative as acceleration measurements for the identification of lower vibration modes in certain applications [24, 25].

Recursive estimation of strain time histories is another common approach. The Kalman Filter has frequently been adopted for state estimation and virtual sensing [26–28]. In this Bayesian estimator a reduced order model, formulated as a set of state-space equations, is used for the estimation of the dynamic state (displacements, velocities, and/or accelerations) of the structure based on measured data (e.g., strains, displacements, accelerations, etc.) [29]. Although Kalman filtering was originally proposed for use based on complete knowledge of the input forces of the structural system [12], several modifications to this algorithm, in which the input could be unknown, have been proposed and validated [30, 31]. In a recent study, accelerations and strains from a truck chassis is used to study the accuracy of an Augmented Kalman Filter (AKF) extended with a fixed-lag smoother and a smoothed joint input-state estimation algorithm. The results of this study show that although strain time histories are affected by a large model error, fatigue life predictions are reliable using both methods [32]. In a very recent work, Tatsis et al.[33] demonstrate the use of substructuring within an AKF for input-state estimation under limited measurement availability. Similarly, Noppe et al. [34] compare the estimated strain time history response of a wind turbine using modal expansion and the AKF. These two methods employ acceleration measurements and a thrust load signal. Results from this study show that time-domain predictions are a good match with the measured response using both techniques with some discrepancies due to discontinuities in the thrust force signal. In addition, predictions in the frequency domain obtained from the AKF demonstrate higher discrepancies than predictions calculated with modal expansion procedures.

In this paper, in-service strain time histories measured from a full-scale rollercoaster structure are used to predict strain time histories at unmeasured locations using both a batch estimation approach and two recursive estimation schemes. A rollercoaster connection was instrumented with four strain rosettes and three orthogonally placed accelerometers. Acceleration measurements are used to verify modal parameters extracted from strain times histories. Due to the complexity of the loading and lack of information to estimate the loading produced by each rollercoaster

passage, output-only methods are suitable for the estimation of strains at unknown locations along with the bracket connection under study. Three methodologies are used for the prediction of strain time histories. A substructure of the instrumented connection is extracted using the Craig–Bampton method. Method 1, referred to as model updating and modal expansion (MUME), makes use of batch data set and conventionally deployed offline methods for modal identification and finite element model updating of a section of the rollercoaster. The NExT-ERA algorithm is used to estimate the modal parameters of the structure. The identified modal parameters are then used to update a FEM of a section of the rollercoaster in conjunction with ANSYS's Workbench's DesignXplorer which employs Kriging and a multi-objective optimization approach [35]. Strain response at unmeasured locations are then estimated in a substructured connection by means of modal expansion procedures based on sparse strain measurements. Confidence bounds on the strain predictions are provided by propagating the estimation uncertainty through modal expansion. In Method 2, the AKF and a substructure of the connection are used, as proposed in a recent work of the authors [36], for real-time estimation. In contrast to past work, the updated model from Method 1 is represented in a state-space formulation and used to determine strains at unmeasured locations using the AKF. In Method 3, the authors propose the use of strain predictions from a control location using modal expansion procedures as new observations in the AKF. Both the modal expansion and the AKF approach can be run in real-time if a model has been first updated and the modal expansion equations have been set up with baseline recordings. An essential distinction between Method 1 and Methods 2–3 lies in the type of estimation that is delivered. In Method 1 the estimation of strain histories is deterministic by definition but extended with the estimation of confidence intervals. In this work, we further offer a strain error estimate based on modal expansion equations for quantifying the uncertainty contained in strain estimates. On the other hand, estimations of the strain histories from the AKF consider model error and noise corruption of observations as stochastic processes into account by virtue of the filter's process and measurement noise. The estimated strain time histories from these approaches are compared with measured data from control locations.

2 Methodology

The passage of a rollercoaster train produces a complex loading pattern on the structure that is hard to measure, model, or predict. The train has seven cars, each car has 4-road wheels, 4-sideguide wheels, and 4-upstop wheels for a total of 12 wheels per car and 78 wheels per train. These wheels are never simultaneously in contact with the rails due to centrifugal forces and the intricate geometry of the structure, which leads to a complex unknown loading pattern. Due to a lack of accurate loading information, output-only methods are deemed essential for the estimation of strains at unknown locations on the connection bracket.

This section presents the approaches used for the estimation of strain time histories at unmeasured locations using response-only measurements. The first method is based on model updating followed by modal expansion (MUME). The second method uses the updated finite element model and the Augmented Kalman filter (AKF) for online estimation of strain time histories at unmeasured locations. The third method, a newly proposed method referred to as modal expansion combined with AKF (ME-AKF), implements predictions from modal expansion into the AKF to improve online predictions.

2.1 Method 1: model updating and modal expansion (MUME)

In this method, natural frequencies and mode shapes are first identified from strain and acceleration time history measurements. Subsequently, the identified natural frequencies are used to calibrate or update the linear elastic finite element model of a section of a rollercoaster. In this research, a Kriging model was also used to create and optimize the structural model. Finally, the modal expansion method is used to predict the strain response at locations of interest as well as error propagation of the estimated strain responses. Figure 1 presents an overview of this process.

2.1.1 Modal identification

NExT-ERA, an output-only or operational modal analysis method, is used to estimate the modal parameters of the structure [37]. In the application of this method, the cross-correlation function of all measurements with a reference channel is first estimated using the inverse Fourier transform of the corresponding cross-spectral density functions. Then, the eigensystem realization algorithm (ERA) is used to realize a mathematical model of the system in state-space using the estimated cross-correlation function previously obtained. Finally, the natural frequencies, mode shapes and damping ratios of the system are extracted from state and measurement matrices. The case study presented makes use of stabilization diagrams to determine the model order [38]. These diagrams allow for the visualization of natural frequencies (or poles) as a function of model order. An identified mode is deemed stable and physical if the natural frequencies do not vary for increasing model orders.

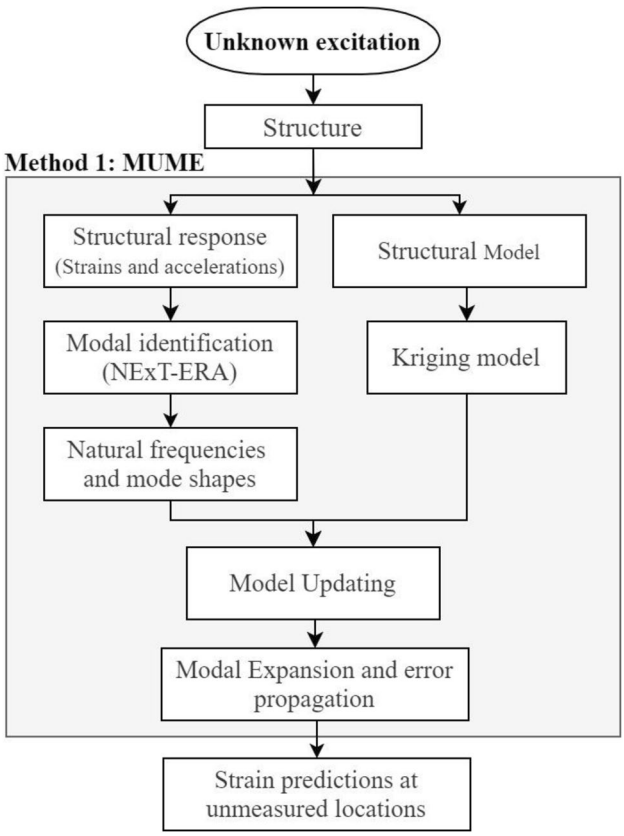

Fig. 1 Method 1. MUME method overview

2.1.2 Model updating

The expected outcome of the model updating process is a finite element model that reliably represents the measured data. In this study, ANSYS Workbench was used to model the structure and update the model. The DesignXplorer [35] module of ANSYS was employed to create and optimize a Kriging model. The use of this module allowed for the evaluation of parameter sensitivity while providing a better understanding of the structure at a little computational cost.

The use of a Kriging model allows for efficient optimization of the difference between the model-predicted and identified natural frequencies obtained from measurements. Kriging relates the updating model parameters with model outputs using a small number of training data sets. Prior to the creation of a kriging model a set of sampling points was generated to cover the design space. This process is referred as Design of Experiments (DOE). There are several DOE algorithms available in engineering literature such as Monte Carlo methods, Latin Hypercube and Central Composite Design (CCD) [39]. These methods generate a group of sampling points such that the space of random input parameters is explored in the most efficient way [40]. The central composite design of experiments algorithm is used to create the Kriging model. The Central Composite Design (CCD) algorithm has been found to be effective when used in large-scale finite element models when evaluating structural dynamics [41–43]. This method combines one center point, points along the axis of the input parameters, and the points determined by a fractional factorial design [35]. This algorithm determines the overall trend of the FE model using the stiffness of longitudinal springs located at the left and right ends of the section of the rollercoaster (input parameters) and the natural frequencies (output parameter) obtained from modal analysis. Once a Kriging model was defined, a multi-objective genetic algorithm was used for the optimization process. Longitudinal spring stiffnesses at the end cross-sections of the rollercoaster (3 at each end) are obtained as a result of the optimization process. Once a reliable model is built, estimates of strains or dynamic behavior at unmeasured locations can be inferred [8, 44].

2.1.3 Modal expansion and error propagation

In this method, estimation of strain time histories at unmeasured locations makes use of the updated FEM and the modal expansion approach. Strain time histories $\boldsymbol{\varepsilon}(t)$ can be calculated as a linear combination of strain mode shapes and strain modal contribution time histories as,

$$\boldsymbol{\varepsilon}(\mathrm{t}) = \boldsymbol{\Phi}_{\varepsilon}\boldsymbol{q}_{\varepsilon}(\mathrm{t}) \tag{1}$$

where $\boldsymbol{\Phi}_{\varepsilon}$ is the strain mode shape matrix and $\boldsymbol{q}_{\varepsilon}(t)$ are the response strains time histories in modal coordinates. Using a modal expansion approach, the strain mode shape matrix can be written as a subset of measured (subscript m) and predicted (subscript p) degrees of freedom (DOF): $\boldsymbol{\Phi}_{\varepsilon} = \begin{bmatrix} \Phi_{\varepsilon,m} \\ \Phi_{\varepsilon,p} \end{bmatrix}$. If there is a good correlation between the updated FEM and identified modal parameters, measured strains can be used to determine $\mathbf{q}_{\varepsilon}(t)$ and estimate structural response at predicted DOFs.

$$\boldsymbol{\varepsilon}_m(t) = \boldsymbol{\Phi}_{\varepsilon,m}\hat{\mathbf{q}}_{\varepsilon}(t) \tag{2}$$

$$\hat{\mathbf{q}}_{\varepsilon}(t) = \left(\Phi_{\varepsilon,m}^{T}\Phi_{\varepsilon,m}\right)^{-1}\Phi_{\varepsilon,m}^{T}\boldsymbol{\varepsilon}_m(t) = \Phi_{\varepsilon,m}^{+}\boldsymbol{\varepsilon}_m(t) \tag{3}$$

$$\hat{\boldsymbol{\varepsilon}}_p(t) = \Phi_{\varepsilon,p}\Phi_{\varepsilon,m}^{+}\boldsymbol{\varepsilon}_m(t) \tag{4}$$

where $\hat{\boldsymbol{\varepsilon}}_p(t)$ are the estimated strains using mode shapes of the updated FEM. Error inhered to mathematical simplifications or measurements can cause estimated strains to deviate from reality.

$$\boldsymbol{\varepsilon}_p(t) = \hat{\boldsymbol{\varepsilon}}_p(t) + \delta\boldsymbol{\varepsilon}_p \tag{5}$$

where $\boldsymbol{\delta\varepsilon}_p$ is the strain estimation error and is assumed to follow a zero-mean normal distribution $N\left(0, \sigma_{\varepsilon_p}\right)$. Strain estimation errors are approximated in this study using the residuals at measured DOFs. These residuals are defined as the difference between measurements and those using the estimated modal response $\hat{\mathbf{q}}_\varepsilon(t)$.

$$\mathbf{r_m}(t) = \hat{\boldsymbol{\varepsilon}}_m(t) - \boldsymbol{\varepsilon}_m(t) \tag{6}$$

$$\boldsymbol{\delta\varepsilon}_p(t) = \frac{\sum_{i=1}^{N_m} r_m(t)}{N_m} \tag{7}$$

where $\mathbf{r}_m$ is the residual between estimated strains at measured DOFs $\hat{\boldsymbol{\varepsilon}}_{\boldsymbol{m}}(\boldsymbol{t})$ and actual measured strain time histories at measured DOFs $\boldsymbol{\varepsilon}_{\boldsymbol{m}}(\boldsymbol{t})$. N_m is the number of measured DOFs. The strain estimation error is approximated as the average of residuals at all measured DOFs. The error standard deviation σ_{ε_p} is then estimated as the standard deviation of $\boldsymbol{\delta\varepsilon}_p(t)$ over a considered time window and is used to set confidence intervals on strain predictions. This method is implemented using a limited set of measured time histories of strains in a rollercoaster connection. Implementation procedures and resulting strain prediction are described in upcoming sections.

2.2 Method 2: augmented kalman filter (AKF)

In this recursive estimation method, the AKF is used, as proposed in previous research [36] and its predicted strains are compared against MUME. The AKF and MUME comprise inherently different functionalities. Method 1 or MUME is more suited for offline or batch estimation, whereas Method 2 or AKF aims to be implemented for real-time estimation. The updated model in Method 1, is used to determine strains at unmeasured location using the AKF with a substructuring approach. Figure 2 presents a flowchart of the method subsequently discussed. A support bracket of a rollercoaster connection is represented in state-space formulation. The prediction of strains within the substructure is then performed using the AKF, a substructured model, and based on a limited number of noisy measurements of strain.

The instrumented connection of the rollercoaster is represented in state-space formulation of the dynamic equations.

$$\mathbf{x}_{k+1} = \mathbf{A}\mathbf{x}_k + \mathbf{B}\mathbf{p}_k + \mathbf{w}_k \tag{8}$$

$$\mathbf{y}_k = \mathbf{G}\mathbf{x}_k + \mathbf{J}\mathbf{p}_k + \mathbf{v}_k \tag{9}$$

where,$k = 1, \ldots, N$ is the time step, $\mathbf{x}_k$ is the state vector (displacements and velocities),$\mathbf{y}(t)$ are the measured response quantities, matrices A, B, G, and J, are the discrete-time state space matrices [45]. Given that in this research strain measurements are collected, instead of

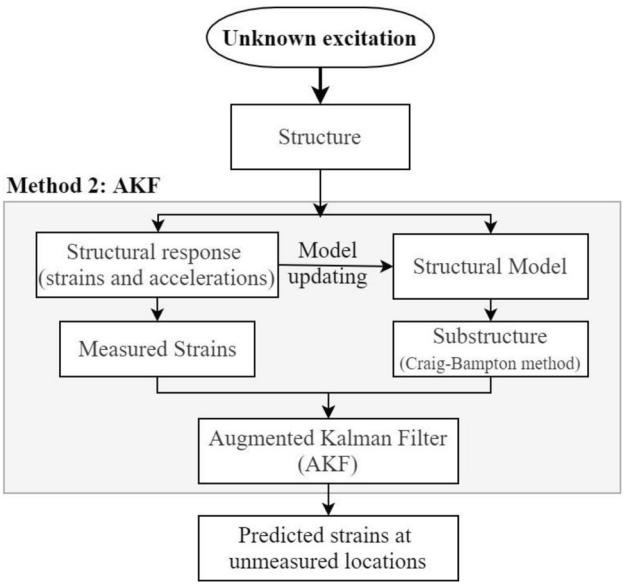

Fig. 2 Method 2. Flowchart of AKF method

displacement measurements, matrix G is pre-multiplied by the displacement differential matrix for the DOFs of interest, $\{\boldsymbol{\varepsilon}\} = [\mathbf{T}]\{\mathbf{u}\}$. Where matrix T can be obtained by differentiation of displacements expressed through shape functions and nodal displacements of a finite element [46]. In doing so, strain measurements can be directly implemented in the AKF algorithm. Random vectors $\mathbf{w}_k$ and $\mathbf{v}_k$, represent the process and measurement noise, respectively. These noise terms are assumed to be mutually uncorrelated, zero-mean, white noise signals with known covariance matrices $\mathbf{Q}$ and $\mathbf{R}$, respectively. Vector $\mathbf{p}_k$ contains the excitation or input forces acting on the substructure's boundaries. Input forces are defined at the connection surfaces of the substructure. In the instrumented rollercoaster connection input forces are located at the two side surfaces, connecting the bracket to the rails, and the bottom surface, connecting the bracket to the main girder. Interface forces are considered in the X, Y, and Z global directions. Additional force constraints are imposed at each interface to reduce the number of estimated forces to a total of 9 forces, 3 forces at each boundary joint, corresponding to each global direction. Having a single resultant in each direction for each interface avoids ill-conditioning of the estimation.

The prediction of strains within the substructure is based on a sparse number of measured strain time histories. Given that the driving forces of the substructure dynamics are unknown, the state is augmented with the input vector to form the so-called augmented state vector $\mathbf{x}_k^{\mathrm{a}} = \begin{bmatrix} \mathbf{x}_k \\ \mathbf{p}_k \end{bmatrix}$. Similarly, the process noise is augmented to $\mathbf{w}_k^{\mathrm{a}} = \begin{bmatrix} \mathbf{w}_k \\ \mathbf{w}_k^{\mathbf{p}} \end{bmatrix}$, where

$\mathbf{w}_k^{\mathbf{p}}$ represents the process noise of the input. Therefore, the input estimation is through the following representation [47],

$$\mathbf{x}_{k+1}^{a} = \mathbf{A}^{a}\mathbf{x}_{k}^{a} + \mathbf{w}_{k}^{a} \tag{10}$$

$$\mathbf{y}_k = \mathbf{G}^{a}\mathbf{x}_{k}^{a} + \mathbf{v}_k \tag{11}$$

where $\mathbf{A}^{a}$ and $\mathbf{G}^{a}$ designate the augmented system and output matrices respectively, written as,

$$\mathbf{A}^{a} = \begin{bmatrix} \mathbf{A} & \mathbf{B} \\ \mathbf{0} & \mathbf{I} \end{bmatrix} \tag{12}$$

$$\mathbf{G}^{a} = \begin{bmatrix} \mathbf{G} & \mathbf{J} \end{bmatrix} \tag{13}$$

A random walk model is here assumed for the evolution of the unknown augmented input. Based on this approach, both input and state are recursively estimated with the standard Kalman filter algorithm, as shown in Fig. 3. Initial value zero can be assumed as an initial step for the prediction of state and one for the first estimation of the covariance. As shown in further works on joint input-state estimation [30, 48], the input may be reliably reconstructed only at the locations where some measurement exists regardless of the initial value of state assumed. However, the state estimation is reliably estimated due to the availability of the state-space model of the system. In the prediction step, the state is advanced based on the equations of the system, while in the update step, the predicted state is updated through a Bayes formula using the latest strain measurements.

2.3 Method 3: modal expansion and augmented kalman filter (ME-AKF)

This newly proposed method fuses the predicted strain response from modal expansion, while recursively estimating strain time histories using the AKF. Figure 4 presents a flowchart of this method. The proposed ME-AKF assumes that the structure's or substructure's FEM is reliable and

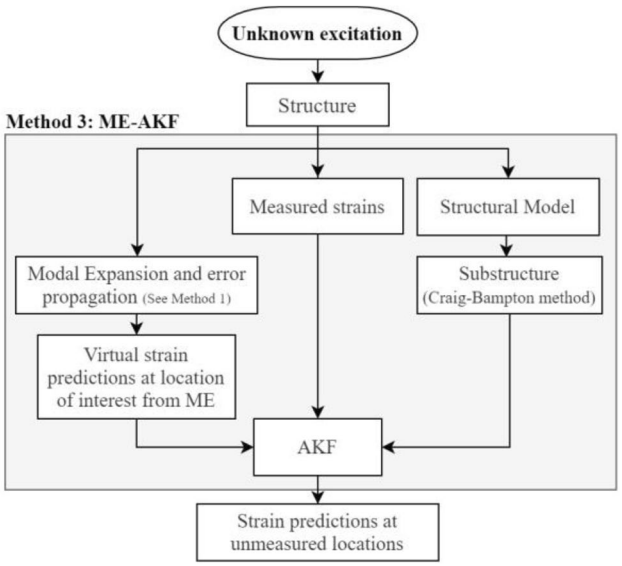

Fig. 4 Method 3. Flowchart of ME-AKF method

that predictions obtained from modal expansion equations are within a reasonable confidence interval. Virtual strain prediction obtained from modal expansion are used with actual measured strains in the Kalman Filter in conjunction with the substructure of the rollercoaster connection. Given that the strain mode shape matrix, Φ_{ε}, remains constant over time, for a particular number of predicted DOFs, the state-space model can be modified to include strain predictions from modal expansion as new observations. Equation (11) or the output equation should be modified to reflect the new observations. The modified state-space model is then augmented as shown in Eqs. (12), (13) and subsequently deployed in Fig. 3. It should be highlighted that once the AKF tuning process is concluded, estimates of strains at unmeasured locations can be calculated. Although tuning of the filter is performed offline, the predicted state can be used for online estimations.

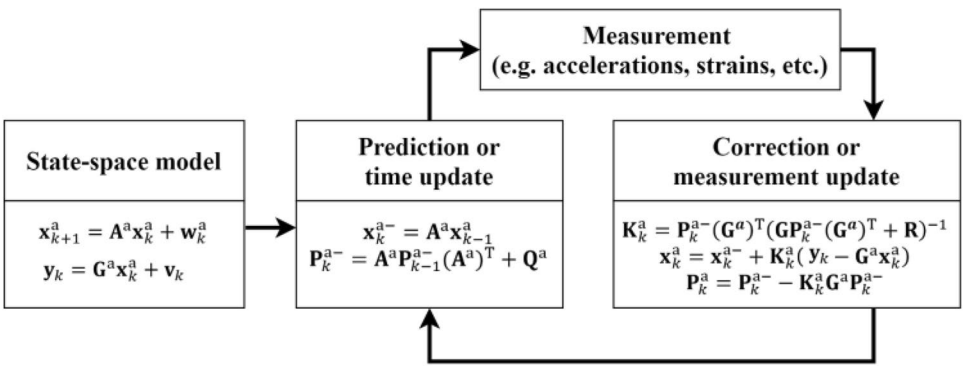

Fig. 3 Augmented Kalman Filter (AKF) Algorithm

3 Case study: rollercoaster structure

3.1 Field testing

For a rollercoaster structure in the US, an instrumentation system including sensors, using battery-powered wireless data acquisition unit, is used to measure the structure's response to moving loads. Strain rosette gauges using quarter arm bridges, accelerometers, thermistors, and an optical sensor were installed on a connection of interest. Figure 5 shows the location of the instrumented connection. The connection consists of a 38.1 mm (1.5 inch) thick steel plate bracket that connects to the main box girder located in the lower part of the rollercoaster's superstructure. This connection is located approximately 10 m (32.8 ft) high and near the midspan between two columns. The span length is approximately 15 m (50 ft). Two circular rails, running along the rollercoaster structure, guide the rollercoaster train. These rails are supported by two ends of the bracket. The rail tubes, the brackets, and the support girder are welded together and made of ASTM A572 grade 50 steel. Data collected at a sampling frequency of 200 Hz, from 10 rides and under a full train service (with 26 water dummies) is used for the estimation of strain time histories in the connection. Water dummies of approximately 50 kg (110 lb) each were used to simulate the average weight of passengers. The total train weight is approximately 11,300 kg (25,000 lb) and contains seven cars with one pilot car. Each car has 4-road wheels, 4-sideguide wheels, and 4-upstop wheels for a total of 12 wheels per car and 87 wheels per train that lead to a complex unknown loading pattern. In addition, the stiffness and damping of the train were not available during testing. Due to the complexity of the loading and lack of information, the authors considered output-only methods as more suitable for the estimation of strains at unknown locations along with the bracket connection.

Fig. 5 Instrumented bracket location with close-up view of bracket and instrumentation

Four strain rosettes were installed at 50.8 mm (2 inches) from the weld toe connecting the bracket to the main girder. Figure 6 shows the strain rosettes installed in the connection. Mean and standard deviations, of data captured by left side the bracket, are shown in Fig. 7. The arms of each strain rosette are color-coded to match the measured response graph line colors shown in Fig. 7. Lighter colors represent strains measured by the left-front strain rosette while darker colors show strains measured by the left-back strain rosette. The optical sensor signal peaks downward when the rollercoaster train arrives and leaves the bracket. Mean values indicate that strains start fluctuating prior to the arrival of

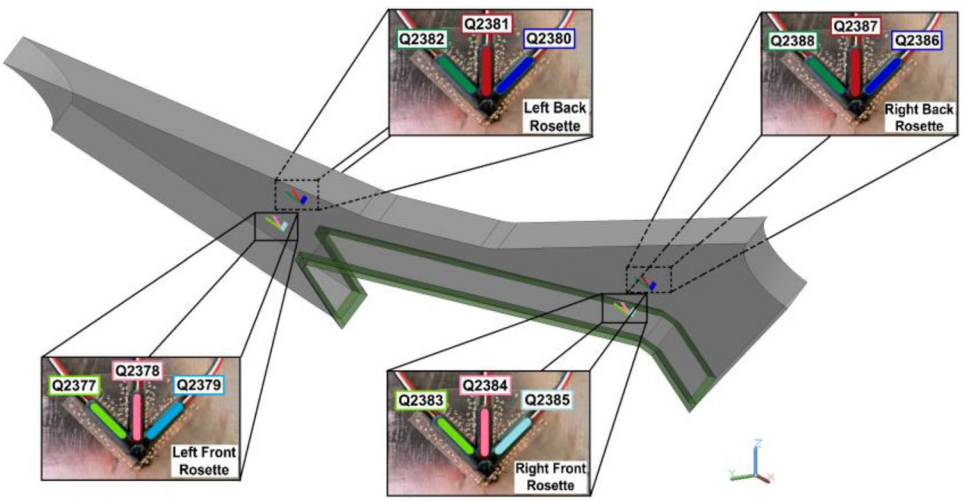

Fig. 6 Strain rosettes installed on the rollercoaster instrumented bracket

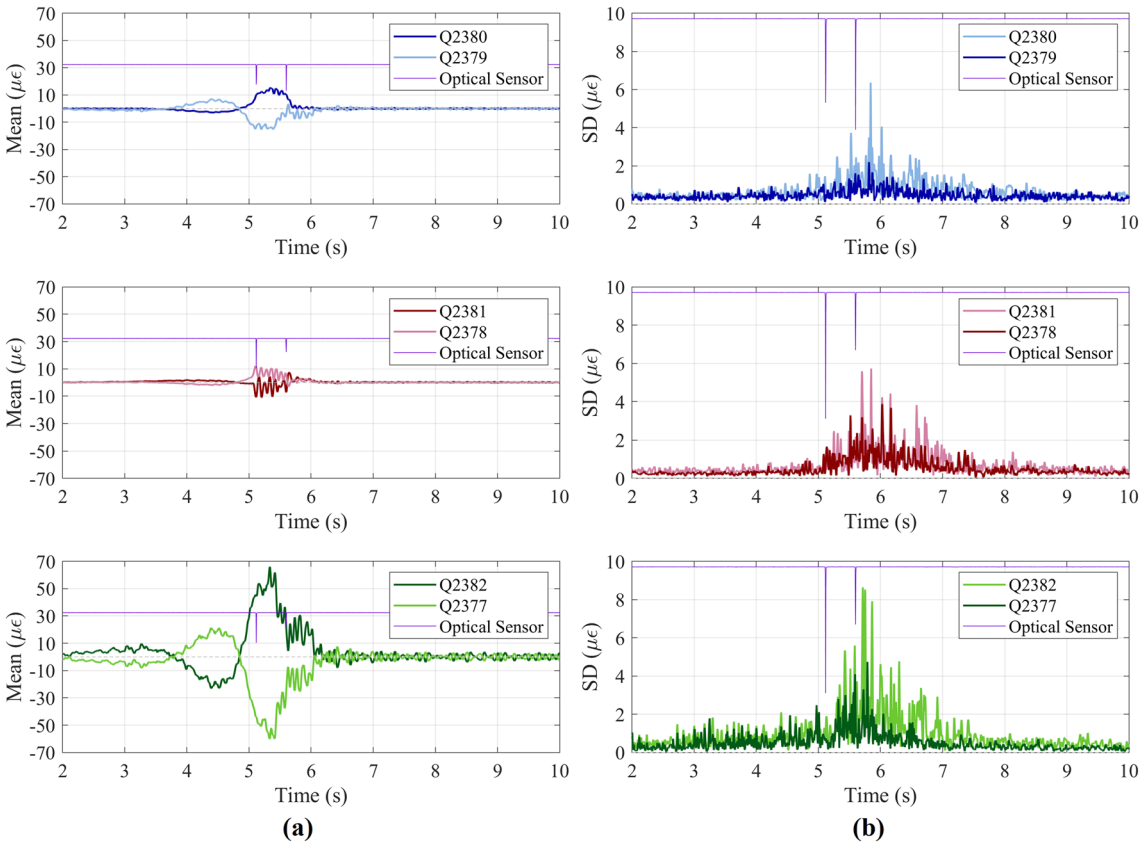

Fig. 7 Strain data from the left-back and left-front rosettes

the train and continue varying after its departure. Standard deviations (SD) of the data collected is in average between one to two microstrains for all loading arrangements on the left-front side and about 6 microstrains in average for the left-back side. Although repeatability between rides might be affected by gravity-driven train speed and axle load distribution, variations are still small in the left-front location. Given the consistency and repeatability of the data captured by this strain rosette, strains captured at this location and for a loading of 26 water dummies are used to validate strain predictions.

Tension and compression strain cycles are evident in all arms of the strain rosette when the train crosses the bracket. In addition, collected strains are mirroring each other in about the same magnitude experiencing tension in one side while compression in the other side of the bracket. Therefore, it is evident that the instrumented bracket is experiencing flexural stresses during each train passage. Furthermore, orthogonal arms experience different magnitude of strains. Peak strain values can differ up to six times.

Accelerometers in three orthogonal (X, Y, and Z) orientations were also placed on the left-back side of the target bracket. Figure 8 shows the raw measured accelerations from a full train passage and the location of accelerometers.

Data from these accelerometers indicate that acceleration measurements increase as the train approaches the bracket, reaching a maximum amplitude right after the train leaves the instrumented bracket. Higher magnitude of accelerations is captured from the accelerometer oriented in the X-axis which is expected given that the instrumented connection is located in a section with vertical and horizontal curvature and little bracing is found in this orientation. Acceleration time histories are used to corroborate natural frequencies identified using strain time histories. Although accelerations are typically used for modal identification, only one set of triaxial accelerometers was mounted on the connection. Thus, limited modal information can be extracted from these set of acceleration measurements.

Signal to noise ratios (SNR) for each arm of the strain rosettes placed on the instrumented connection are calculated to determine the suitability of the stain time histories for estimation of modal parameters. SNR is defined as the ratio of signal power to the noise power calculated in terms of root mean square of the amplitude of the signal and noise time histories [49]. Noise for each strain rosette arm is defined as the data captured for about 14 s after each train passage and for about 88 s. In addition, the signal is defined to start 1.5 s before and end 1.5 s after the train arrival.

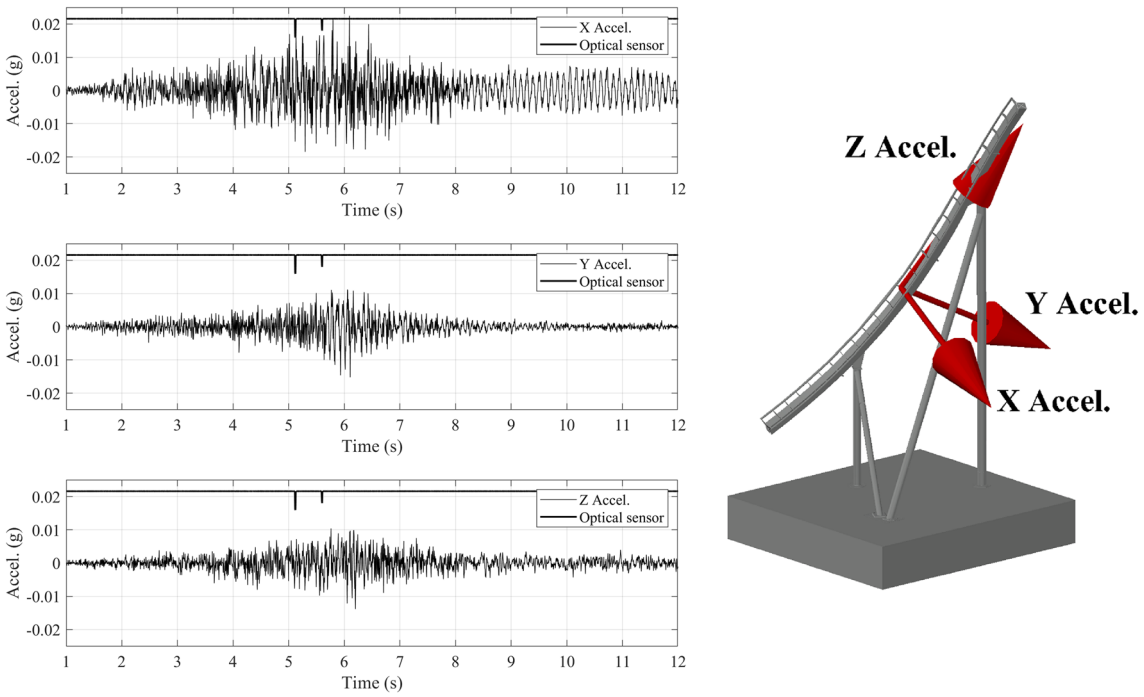

Fig. 8 Acceleration data in time domain and accelerometer orientation in space

Figure 9 show the SNR in dB estimated for all strain rosette arms.

The strain rosette arms that measured higher magnitude signals are characterized by higher SNR values. The left-side locations of the connection comprise overall higher SNR values. Given that strain time histories collected from the middle arms of all rosettes indicate a low SNR, the strains collected from these arms will be excluded from the modal identification and modal expansion processes.

3.2 Finite element model

The complete design or as-built drawings of the rollercoaster structure are not available to the research team. Therefore, a section of the rollercoaster was scanned using Lidar technology. A section of about 30 m (100 ft) of the rollercoaster including the instrumented connection were scanned with a 3D laser scanner to capture overall geometry and a portable Coordinate Measuring Machine (CMM) to more accurately cross-scan a connection and its weld. Figure 10 shows the scanners employed to capture the geometry of the rollercoaster section. The 3D scanner used was the Focus3D X 330. This scanner has a ranging error of ± 2 mm and levels each scan with an accuracy of 0.015° and a range of $\pm 5°$ [50]. In addition, a CMM arm with a precision of ± 0.020 mm and with a 6-Degrees of Freedom (DOF) probe [51] was used to determine in more detail the geometry of the instrumented connection.

After the rollercoaster section was scanned, the obtained point cloud was converted to a CAD model for drafting

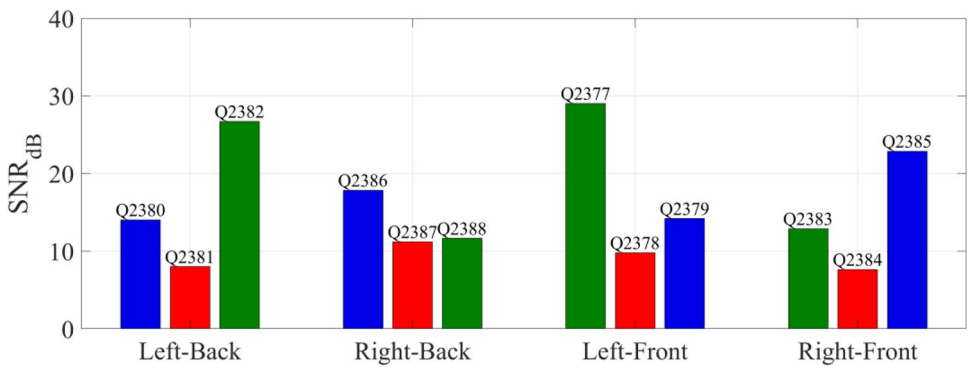

Fig. 9 Signal to noise ratio of measured strain rosette time histories

Fig. 10 Scanning of rollercoaster section. Top: 3D LiDAR Scanner. Bottom: CMM arm

and simplification prior to importing to ANSYS. Figure 11 shows the finite element model of the section of the rollercoaster. The arrow shows the location of the instrumented bracket. A combination of frame, shell and solid elements are used for finite element modeling. Rails and columns of the rollercoaster are modeled using frame elements. The main girder running along the rollercoaster is a box girder modeled using shell elements. Due to the vertical and horizontal changes in curvature along the structure, the additional DOFs provided by 8-node shell elements were deemed necessary when creating the model. Brackets connecting the main girder to the rails are modeled using 20-node solid elements. Due to the complexity of the geometry a combination of square and triangular or tetrahedral shape elements is used in the model. ASTM A572 grade 50 steel is assigned to all elements of the rollercoasters.

A finer mesh is used for brackets closer to the instrumented connection. The instrumented connection includes additional weld elements modeled with 20-node solid elements directly connected to the bracket solid elements. Connection between railings and brackets is ensured through rigid links connected to all contact nodes on sides of the brackets in contact with the railings. The rollercoaster's upright support columns are fixed at the base. In addition, the rollercoaster's left and right ends are constrained with three longitudinal springs which orientations are aligned with the principal axes of the ends of the rollercoaster's cross-section. To reduce the number of unknown parameters, all degrees of freedom at each termination point were coupled to one node at the centroid of the termination point with six DOFs. A sensitivity analysis of the stiffness parameters at termination points showed that natural frequencies of the rollercoaster had little correlation to rotational springs. Therefore, only three translational springs aligned with the principle axes of the end cross-sections were used at each

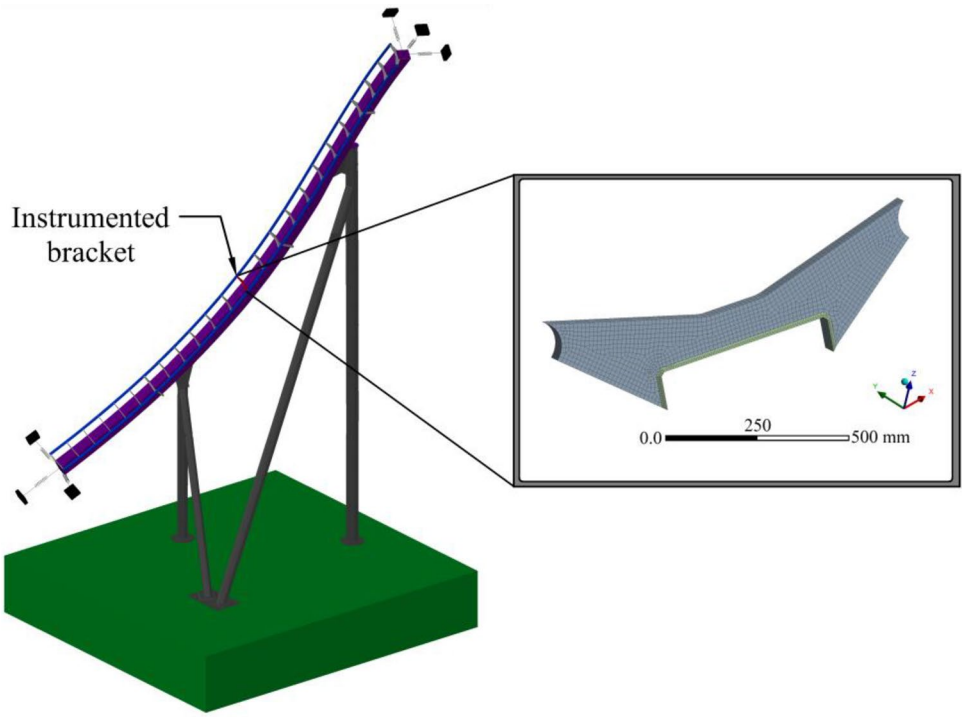

Fig. 11 Rollercoaster Section Model and close-up view of instrumented bracket FEM mesh

termination point of the rollercoaster. A total of six linear spring stiffnesses (three at each end) are used as updating parameters of the FE model of the rollercoaster section to improve the analytical natural frequencies compared to the measured ones.

3.2.1 Connection substructure

The analysis of complex and large structures, such as rollercoasters, can be simplified by substructuring the component of interest. Dynamic substructuring allows for fast analysis of a substructure without the need of re-analyzing the entire structure [52]. Model updating as well as Bayesian filtering algorithms are computationally demanding due to the large size of the Finite Element Models under study. Component Mode Synthesis techniques (CMS) use component modes and characteristic interface modes to characterize the dynamic behavior of a substructure [53]. One of the most commonly adopted techniques is the Craig-Bampton method. This method assumes that a finite element model can be divided into substructures in which only interface degrees of freedom (DOFs) belong to more than one substructure, making each substructure linearly dependent. The outcome of this method is a set of relatively low-dimensional stiffness and mass matrices, which contain the natural frequency, and mode shape information of the structure[54]. The deployment of the Craig Bampton method in large structures, such as bridges and wind turbines, has shown to reduce the computational effort by more than three orders of magnitude while maintaining the accuracy of the model [55–57]. The method requires to partition the substructure into boundary and internal degrees of freedom. The dynamic behavior of the substructure is represented by the following equation of motion,

$$\begin{bmatrix} \mathbf{M}_{bb} & \mathbf{M}_{bi} \\ \mathbf{M}_{ib} & \mathbf{M}_{ii} \end{bmatrix} \begin{bmatrix} \ddot{\mathbf{u}}_b \\ \ddot{\mathbf{u}}_i \end{bmatrix} + \begin{bmatrix} \mathbf{C}_{bb} & \mathbf{C}_{bi} \\ \mathbf{C}_{ib} & \mathbf{C}_{ii} \end{bmatrix} \begin{bmatrix} \dot{\mathbf{u}}_b \\ \dot{\mathbf{u}}_i \end{bmatrix} + \begin{bmatrix} \mathbf{K}_{bb} & \mathbf{K}_{bi} \\ \mathbf{K}_{ib} & \mathbf{K}_{ii} \end{bmatrix} \begin{bmatrix} \mathbf{u}_b \\ \mathbf{u}_i \end{bmatrix} = \begin{bmatrix} \mathbf{f}_b \\ \mathbf{f}_i \end{bmatrix} \tag{14}$$

where **M**, **C** and **K** correspond to mass, damping, and stiffness matrices respectively. **u** is the displacement vector and **f** is the force exciting the system over time. Single and double dot accents correspond to first and second time-derivatives of displacement, respectively. Subscripts 'b' corresponds to the boundary or interface degrees of freedom (DOFs) and subscripts 'i' refer to the internal DOFs of the substructure.

The physical coordinates can be transformed into Craig–Bampton coordinates by the following transformation,

$$\begin{bmatrix} \mathbf{u}_b \\ \mathbf{u}_i \end{bmatrix} = \begin{bmatrix} \mathbf{B}_{cm} & \mathbf{\Phi} \end{bmatrix} \begin{bmatrix} \mathbf{u}_b \\ \mathbf{q}_m \end{bmatrix} = \begin{bmatrix} \mathbf{I} & \mathbf{0} \\ \mathbf{\Phi}_b & \mathbf{\Phi}_i \end{bmatrix} \begin{bmatrix} \mathbf{u}_b \\ \mathbf{q}_m \end{bmatrix} = \mathbf{T}_{\mathbf{CB}} \begin{bmatrix} \mathbf{u}_b \\ \mathbf{q}_m \end{bmatrix} \tag{15}$$

The first column partition of the Craig-Bampton transformation matrix, $\mathbf{B}_{cm}$, relates physical displacements at the boundary to physical displacements of the internal degrees of freedom. This first column partition is usually known as the interface constraint mode matrix where $\mathbf{\Phi}_b = -\mathbf{K}_{ii}^{-1}\mathbf{K}_{ib}$. The second column partition, $\mathbf{\Phi}$, contains the fixed-base mode shapes. This partition can be physically interpreted as the displacements of the internal degrees of freedom relative to the displaced boundary. $\mathbf{\Phi}_I$ are the mode shapes of the constrained substructure while $\mathbf{q}_m$ corresponds to the generalized modal displacements and contains only the solution for the most significant modes. This truncation is justified by the small contribution of the response in higher frequency modes.

By initially substituting Eq. (2) in Eq. (1) and subsequently by means of a Galerkin projection, the equation of motion for the substructure can be written as follows,

$$\begin{bmatrix} \mathbf{B}_{cm}^T\mathbf{M}\mathbf{\Phi} & \mathbf{B}_{cm}^T\mathbf{M}\mathbf{\Phi} \\ \mathbf{\Phi}^T\mathbf{M}\mathbf{B}_{cm} & \mathbf{\Phi}^T M\mathbf{\Phi} \end{bmatrix} \begin{bmatrix} \ddot{\mathbf{u}}_b \\ \ddot{\mathbf{q}}_m \end{bmatrix} + \begin{bmatrix} \mathbf{B}_{cm}^T\mathbf{C}\mathbf{\Phi} & \mathbf{0} \\ \mathbf{0} & \mathbf{\Phi}^T\mathbf{C}\mathbf{\Phi} \end{bmatrix} \begin{bmatrix} \dot{\mathbf{u}}_b \\ \dot{\mathbf{q}}_m \end{bmatrix} + \begin{bmatrix} \mathbf{B}_{cm}^T\mathbf{K}\mathbf{\Phi} & \mathbf{0} \\ \mathbf{0} & \mathbf{\Phi}^T\mathbf{K}\mathbf{\Phi} \end{bmatrix} \begin{bmatrix} \mathbf{u}_b \\ \mathbf{q}_m \end{bmatrix} = \begin{bmatrix} \mathbf{f}_b + \mathbf{\Phi}_b^T\mathbf{f}_i \\ \mathbf{\Phi}_b^T f_i \end{bmatrix} \tag{16}$$

or in a compact form:

$$\tilde{\mathbf{M}}\ddot{\tilde{\mathbf{u}}}(t) + \tilde{\mathbf{C}}\dot{\tilde{\mathbf{u}}}(t) + \tilde{\mathbf{K}}\tilde{\mathbf{u}}(t) = \tilde{\mathbf{f}}(t) \tag{17}$$

The dimension of the reduced system matrices $\tilde{\boldsymbol{M}}$, $\tilde{\mathbf{C}}$, and$\tilde{\mathbf{K}}$ equals to the number of boundary DOFs plus the number of modes retained for the internal DOFs. Equation (4) is used to estimate the modal response of the substructure (i.e., natural frequencies and strain mode shapes) and state estimation of the substructure (i.e. displacements, velocities, and accelerations) when employed in the AKF.

The rollercoaster in this study is substructured, using the Craig-Bampton method, by partitioning the bracket of interest and its weld from the rails and the main rollercoaster box girder. Boundary nodes are defined to be those intersecting the instrumented bracket and rails as well as those intersecting the main girder and the bracket, while the remaining nodes are considered as internal nodes. The resulting substructure is shown as a close-up view in Fig. 11. The model was reduced from 80,165 nodes for the entire modeled structure to 25,854 nodes in the substructure and from 27,421 to 4,842 solid elements. Model updating is performed for the overall rollercoaster model. The substructure model of the monitored bracket and its weld are used for modal expansion implementation and in the AKF framework for estimation of strains at unmeasured locations on the bracket.

4 Case study: strain predictions

4.1 Method 1: MUME

This section provides the strain predictions via the model updating and modal expansion (MUME) method. Natural frequencies and mode shapes are first identified from strain time histories and verified with acceleration time histories. Then, identified natural frequencies are used to calibrate the linear elastic Finite Element Model of a section of a rollercoaster. The calibrated model is finally used in the modal expansion method to estimate the strain time histories at unmeasured DOFs.

4.1.1 Signal processing and modal identification

Measured raw strains and accelerations are first filtered to reduce noise contamination in modal parameter estimates. Data cleansing involves the removal of voltage spikes and filtering. A total of approximately 17 min of data at a frequency sampling of 200 Hz are used. Table 1 presents a summary of processing procedures used for strain and acceleration data prior to modal identification.

Power spectral density functions of measured strains and accelerations are shown in Figs. 12 and 13, respectively. Strain rosette arms with higher SNR values have distinctive peaks in frequency domain plots. In these plots, peaks indicate the natural frequencies of the rollercoaster. Correspondingly, middle arms (Q2381, Q2387, Q2378, Q2384) provide little energy at the frequency range of interest, thus are excluded from modal identification procedures.

Table 1 Data processing summary

Data type	Pre-filtering manipulation	Filter used
Strains	Observed large outliers and voltage peaks are removed by averaging between adjacent data point	A band pass FIR filter is used in the at 0.1 to 30 Hz
Accelerations	–	A band pass FIR filter is used starting at 2 Hz and ending at 30 Hz. Add window type

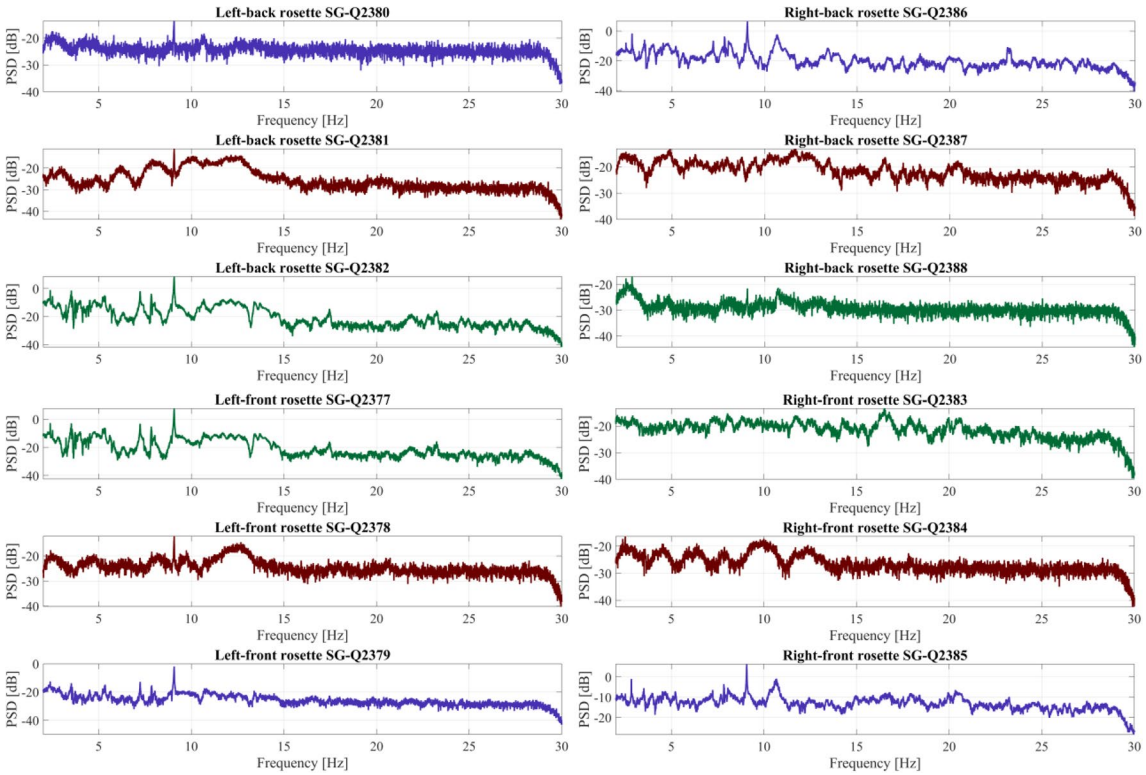

Fig. 12 PSD of measured strains

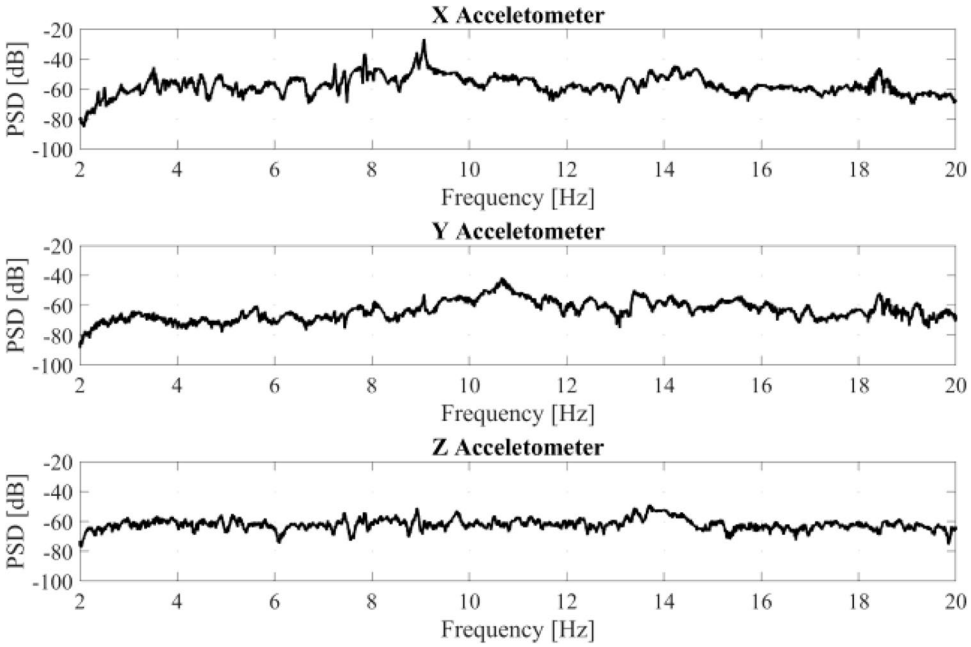

Fig. 13 PSD of measured accelerations

Acceleration data in the frequency domain shows distinctive peaks in data collected in the X-direction and a few peaks in the Y-direction. On the other hand, acceleration data in the Z-direction is discarded due to a lack of significant magnitude in the response experienced in this orientation.

In-service strain and acceleration data recorded under different loading conditions is used to determine the modal properties of the rollercoaster. Modal parameters are estimated using the NExT-ERA methods. The NExT method is employed using the responses of all orthogonal arms of the strain rosettes. Free vibration response of the rollercoaster is estimated using the inverse Fourier transform of cross power spectral densities (CPSD) with hamming windows overlapped 50%. Arm Q2377 from the left front rosette is taken as the reference channel. Data collected from this arm has the highest SNR and clear peaks when plotted in frequency domain. The ERA method is employed to identify the modal parameters of the structure using 2,000 data points (or 10 s) of free vibration data from 8 channels (orthogonal arms of all rosettes) and a 8,000 × 1,000 Hankel matrix. The successful application of this method requires the selection of the order of the state-space model. A stabilization diagram is used to determine the lowest model order that can provide all the modes of interest [58, 59]. Figure 14 shows the stabilization diagram obtained using strain time histories from orthogonal arms of all strain rosettes. Red dotted lines enclose the identified natural frequencies.

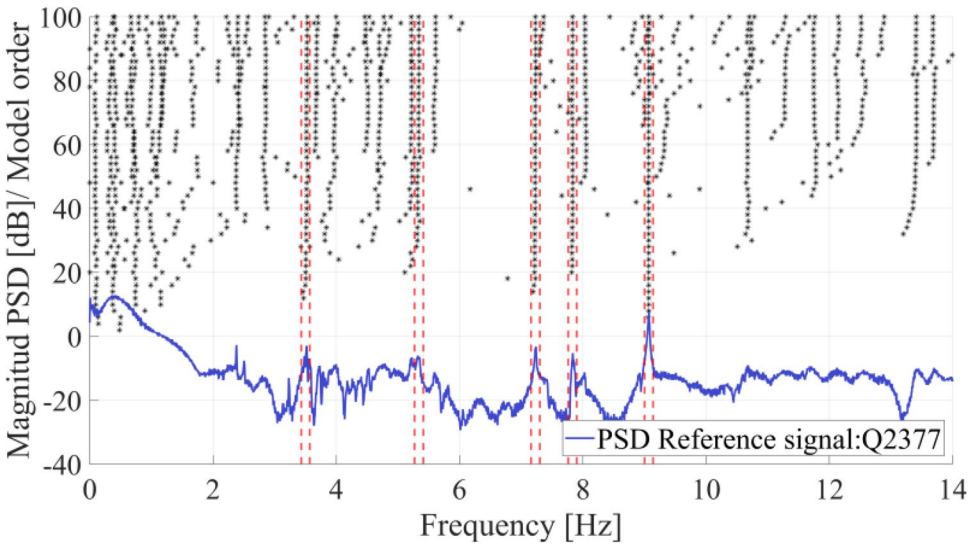

Fig. 14 Strain time histories stabilization diagram

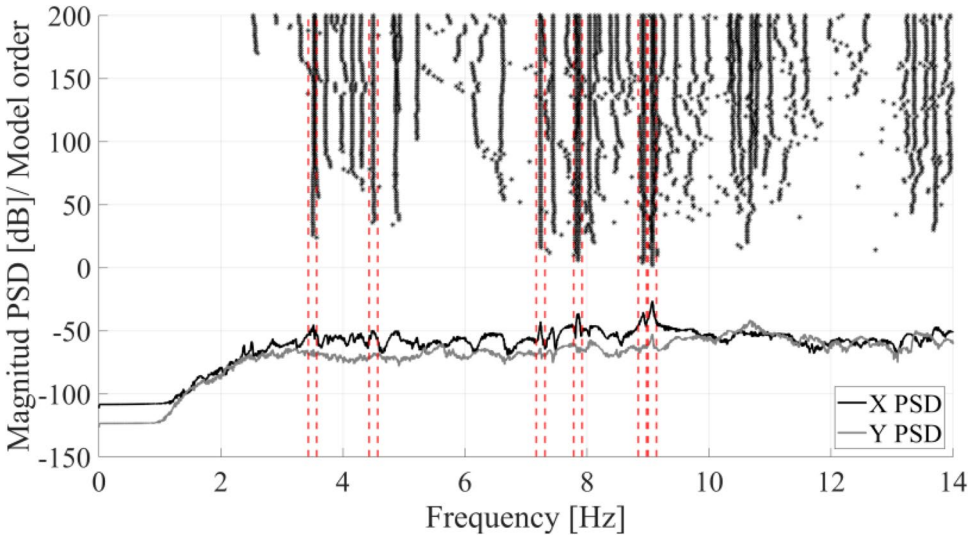

Fig. 15 Acceleration time histories stabilization diagram

Table 2 Identified natural frequencies and damping ratios

From strain data			From acceleration data		
Number	f_n (Hz)	Damping ratios (%)	Number*	f_n (Hz)	Damping ratios (%)
1	3.5	1.43	1	3.5	0.96
–	–	0.54	1[a]	4.5	0.75
2	5.3	–	–	–	–
3	7.2	0.27	3	7.2	0.12
4	7.8	0.21	4	7.8	0.22
–	–	–	5[a]	8.9	0.14
5	9.1	0.13	6	9.1	0.12

*Superscript 'a' highlights additional modes identified with acceleration measurements

Acceleration time histories are used to verify the natural frequencies identified from strain measurements. A stabilization diagram employing data measured by X- and Y-direction accelerometers is presented in Fig. 15. Accelerations from X-direction is used as reference for CPSD.

Based on the stabilization diagrams obtained from both strain and acceleration measured data, the most excited vibration modes are between 3.5 Hz and 9.1 Hz. Some natural frequencies that are visible in the strain-based stabilization diagram are indistinguishable in the acceleration-based diagram and vice-versa. For instance, a clear peak at 5.3 Hz is visible in the strain-based diagram while no peaks are evident at this frequency in the acceleration-based diagram. The differences can be attributed to the location and orientation of the sensors [60]. Table 2 presents the identified natural frequencies and damping ratios using strain and acceleration data. Given that mode shapes are only available from strain time histories, further use of modal parameters for model updating and modal expansion are based only on strain time histories.

4.1.2 FEM updating

Once the natural frequencies of the rollercoaster are identified using measured data, the rollercoaster's FEM is updated to match the natural frequencies shown in Table 2. A Kriging model and the multi-objective algorithm for optimization are implemented to update the six boundary spring stiffness values of the model. The outcome of the optimization process is a FEM representative of the instrumented rollercoaster and adequate for implementation of the methods presented in this research. ANSYS's Workbench's DesignXplorer [35] is deployed for the updating. Mode shapes of the first 7 modes (between 3.5 Hz and 9.1 Hz), obtained after optimization of the left and right boundary conditions of the section of the rollercoaster, are shown in Fig. 16.

FEM strain mode shapes are compared to measured strain shapes in Fig. 17. In this figure, strain mode shape ordinates are stacked sequentially only for visual comparison purposes. Comparison of FEM strain shapes at location of orthogonal arms of the strain rosettes shows good agreement with identified modes at 7.23 Hz and 9.07 Hz. Although other FEM mode shapes show discrepancies with measured counterparts at certain locations, there is still an overall agreement between model and measured strain shapes. Given that strain rosettes on the right side of the bracket have low SNR, arms Q2385 and Q2386 show larger discrepancies between measured and FEM shapes.

Table 3 A comparison of natural frequencies and mode shapes (RMS error and MAC) obtained from measured strains and FEM.

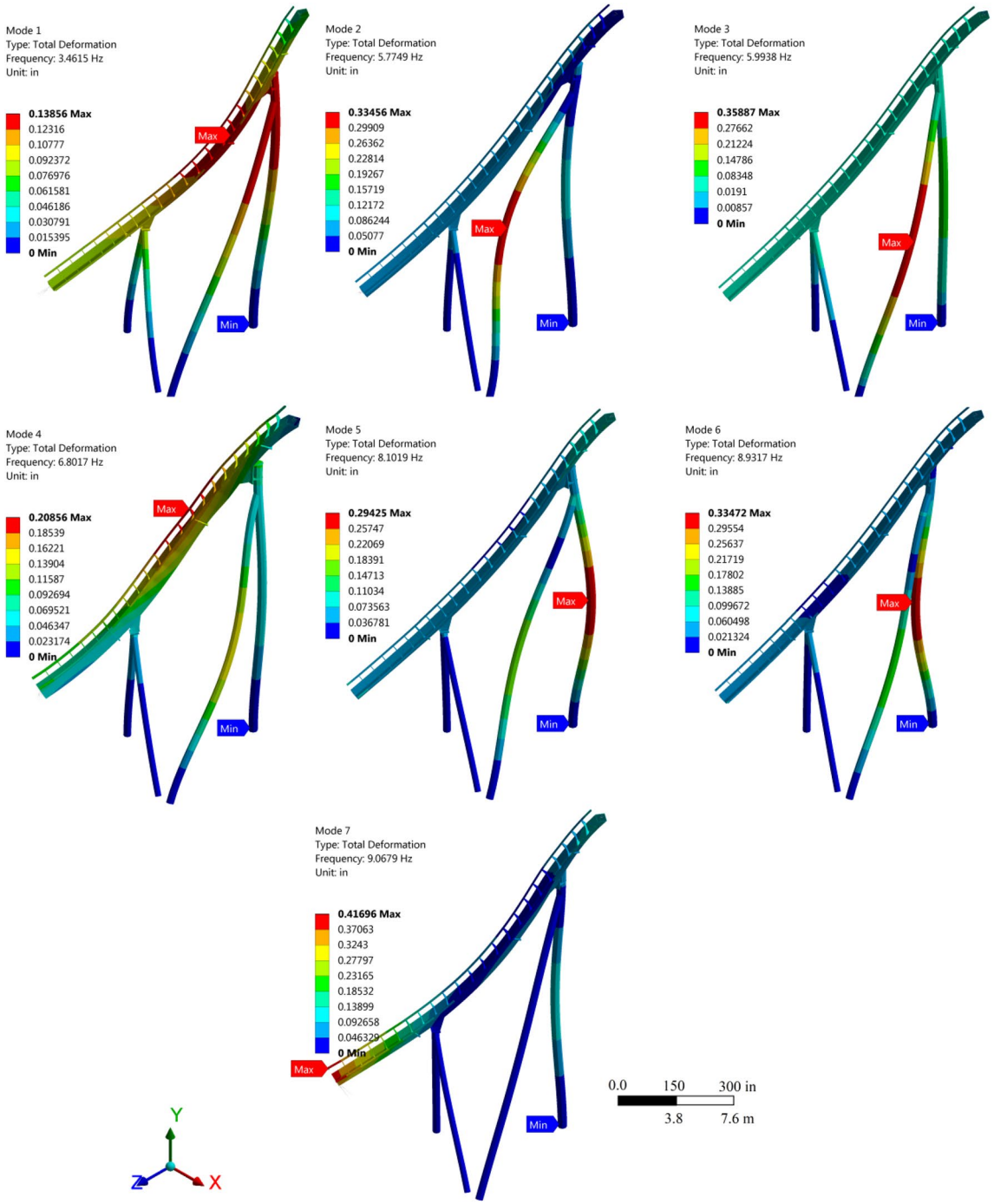

Fig. 16 Natural frequencies and mode shapes from FE model of rollercoaster

Comparison of natural frequencies, f_{error}, show a maximum error in natural frequencies of -7.45% for the second FEM mode of vibration at 5.34 Hz indicating a reasonable match between the FEM and measurements. The largest RMS error and lowest MAC value is found for mode 3 at 7.83 Hz. Although, this mode was initially considered in the model updating process, the low MAC value of 0.10 indicates that identified mode does not correspond to the FEM mode and thus is excluded in further calculations for response prediction. The low modal damping ratios are within the acceptable range for steel structures with without any nonstructural components.

The initial rollercoaster model was used in previous research [36] and resulted in good predictions when the standard AKF was deployed. However, the model updating procedure provides a more reliable FEM for the

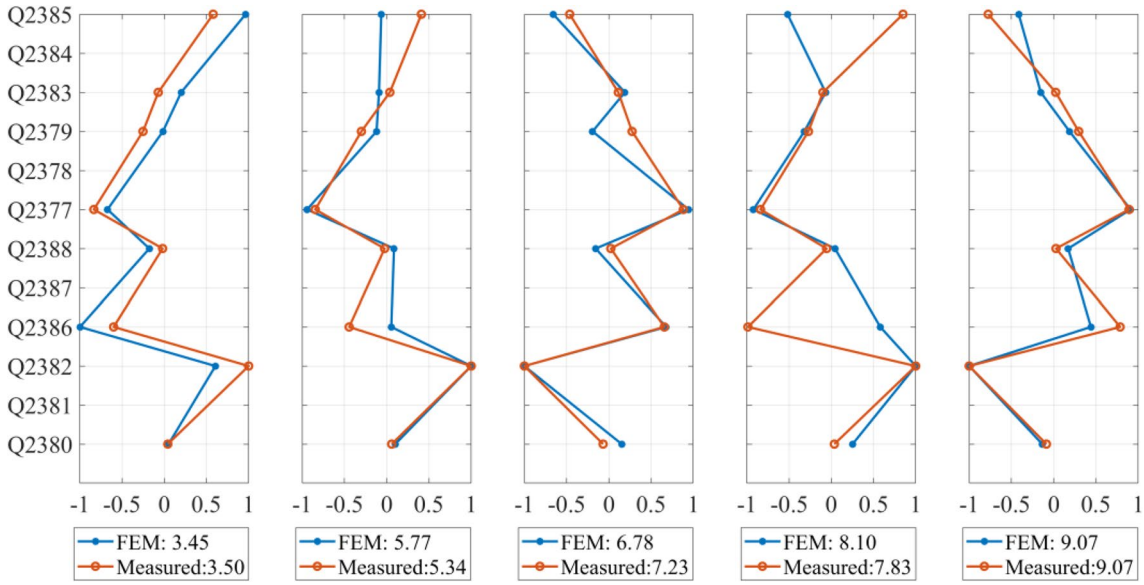

Fig. 17 Mode shapes and natural frequencies from measured strains and FEM

Table 3 Identified natural frequencies and damping ratios vs FEM natural frequencies

From strains measurements			From FEM		f_{error}(%)	RMS_{error}	MAC
Number	Natural frequency (Hz)	Damping ratios (%)	*Number	Natural frequency (Hz)			
1	3.50	1.43	1^{FEM} (1)	3.46	1.45	0.28	0.78
2	5.34	0.54	2^{FEM} (2)	5.77	−7.45	0.26	0.75
–	–	–	3^{FEM}	5.99	–	–	–
3	7.23	0.27	4^{FEM} (3)	6.80	6.64	0.21	0.88
4	7.83	0.21	5^{FEM} (4)	8.10	−3.33	0.74	0.10
–	–	–	6^{FEM}	8.93	–	–	–
5	9.07	0.13	7^{FEM} (5)	9.07	0	0.20	0.91

*Natural frequency number match with measured strain natural frequencies

implementation of the modal expansion. Table 4 presents a comparison between the initial and updated FE model's end stiffnesses and natural frequencies.

4.1.3 Strain predictions and uncertainty quantification

The modal expansion method is used next to predict strains at the left-front strain rosette. Strain mode shapes from the FEM and measurements from strain gauges are used to calculate the strain time history at unmeasured DOFs. Data from the left-front rosette is only used for validation and not employed in the modal expansion procedure. The number of modes considered in the modal expansion process should be less than the number of measurements (sensors) used. Given that not all modes are identified using the measured strain time histories, FEM modes are reorganized to prioritize the better matching modes. The considered modes are 1, 2, 3, and 5. Root mean square (RMS) errors between predicted strains and measured strains at the location of the left-front strain rosette are calculated for several combinations of sensors and the number of modes. Normal and shear strain time histories estimations are generated. Normal strain time histories are taken from orthogonal arms while shear time histories are calculated based on all rosette arms ($\gamma_{xy} = 2\varepsilon_{45°arm} - (\varepsilon_{0°arm} + \varepsilon_{90°arm})$). Fig. 18 shows the RMS error of predicted normal and shear strain time histories while changing the number of measurements and number of modes used for the prediction. For instance, the intersection between three measurements and two FEM mode shapes represent the RMS error obtained for predictions using the three highest quality measurements and the first two matching mode shapes. Quality of measurements used for prediction is based on the SNR previously calculated.

The RMS error calculated for normal and shear predictions is generally lower in the predictions of normal strains. Higher values of error are found overall for the prediction

Table 4 Initial and updated finite element model comparison of spring stiffness and natural frequencies

Spring Stiffness (kN/m)		
Location	Initial	Updated
X right end	10,468	15,715
Y right end	4,422	2,933
Z right end	5,649	6,171
X left end	7,536	2,156
Y left end	50,009	16,610
Z left end	16,490	2,630
Natural Frequencies (Hz)		
Number	Initial	*Updated
1^{FEM}	4.36	3.46 (1)
2^{FEM}	5.95	5.77 (2)
3^{FEM}	6.27	5.99
4^{FEM}	7.34	6.80 (3)
5^{FEM}	8.36	8.10
6^{FEM}	8.99	8.93
7^{FEM}	10.68	9.07 (5)

*Natural frequency number match with measured strain natural frequencies

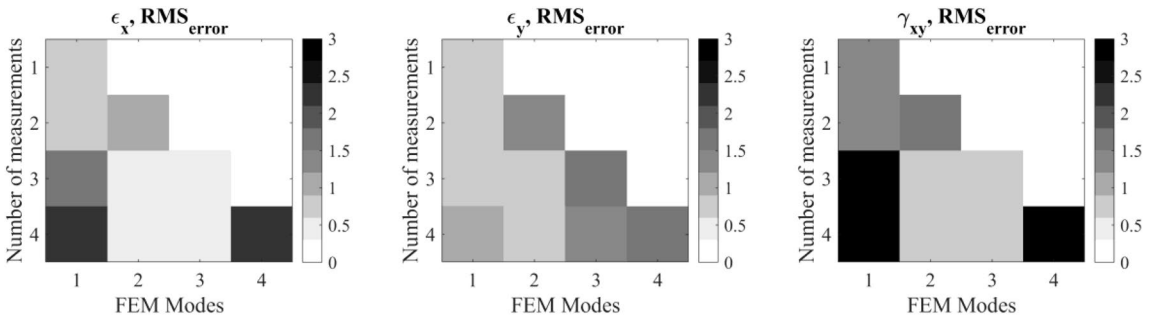

Fig. 18 RMS error for ε_x, ε_y, and γ_{xy} strain history predictions for the left-front strain rosette

of shear strains compared to normal strains. Considering that shear strains are calculated based on strain data collected from all arms of the rosette, noise from these sensors will be reflected in these calculations affecting predictions and RMS error values. Accuracy in the predictions is highly dependent on the quality of the data and the reliability of the FEM. Therefore, adding noisy measurements with low SNR will increase the prediction error. Best predictions are computed when the first three modes (modes 1, 2, 3) are used in conjunction with the 3 to 4 sensors/measurements with the highest SNR.

Predicted strains at the left-front side of the instrumented connection from two case scenarios are shown in Fig. 19. The predicted strains from Case 1 scenario use modes 1, and 2 together with the following three measured strain time histories: at left-back ε_x strain (Q2382), left-back shear strain (calculated using Q2380, Q2381, and Q2382), and right-back shear strain (calculated using Q2386, Q2387, and Q2388). Predictions corresponding to Case 2 scenario using modes 1, 2, and 3 together with the same three measured strain time histories used in Case 1. These two case scenarios correspond to the lowest RMS errors among normal and shear strain predictions. Case 1 scenario yields an average RMS error of 0.65 με, while Case 2 has an average error of 0.98 με.

Predicted strains from both cases seem to efficiently predict the overall behavior of ε_x and γ_{xy} strains and closely correlate to measured strains. Larger errors are observed in predicted ε_y strains (Q2379) for Case 2. Although an additional FEM mode was included in this case, Q2379 shows a larger difference between measured mode shape and FEM mode shape. In addition, the magnitude of strains measured and SNR values by this strain rosette arm are considerably lower compared to ε_x strains (Q2377) and the shear strains.

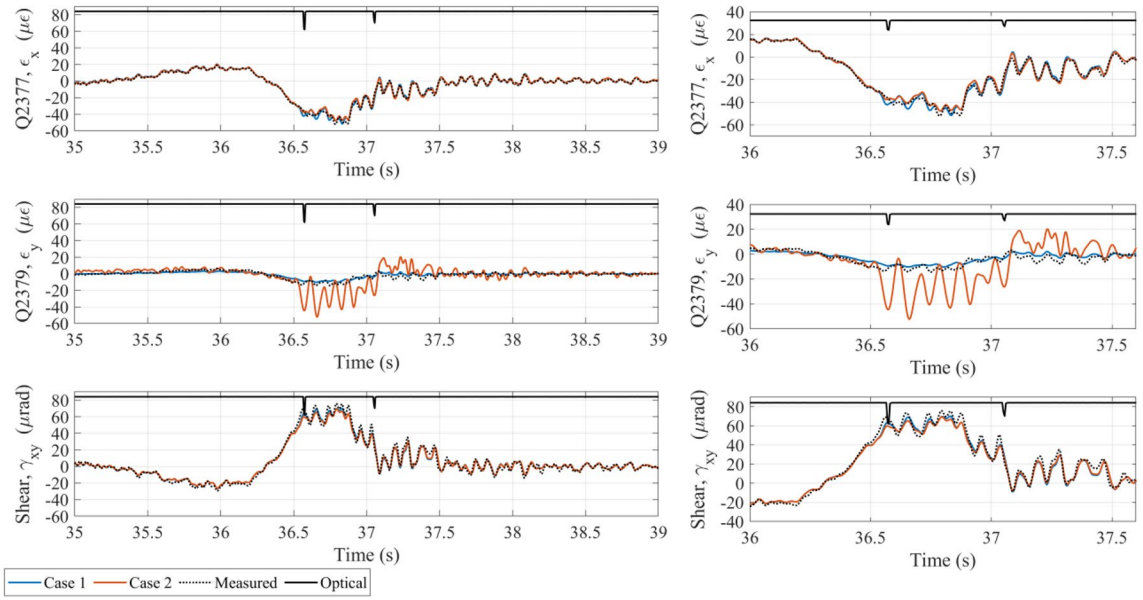

Fig. 19 Comparison of strain predictions using different number of modes in MUME. Overall view and close-up view

It is therefore likely that the inherent measurement noise can be more prominently affecting these signal readings. Case 1 predictions of ε_x, ε_y, and γ_{xy} strains lie closer to the measured strains. Given that shear strains are calculated based on measurements from all arms of a strain rosette, deviations in shear strain predictions can be attributed to accumulated error from measuring gauges. Although both case scenarios succeed at predicting the ε_x and γ_{xy} strains, Case 1 estimates of strains show better overall fit.

The uncertainty of predicted strains is calculated for Case 1 using Eqs. (2) and (3). The measured DOFs are used to back-calculate the strain modal coordinates at each time. Given the non-stationary nature of the signal, the error is also expected to be non-stationary and therefore, the response time history is divided into four zones assuming constant error variance at each zone. Each zone is defined based on the magnitude of strains measured. Zones 1 and 4 occur before and after train passage, respectively. Zone 2 starts about 3 s before train arrival and ends about a second before train arrival. Although during this time zone some preceding strains exist due to the train passage, these lie outside the dominant strains zone. Zone 3 includes strains occurring due to a train passage and its aftermath. It starts about a second before train arrival and ends about two seconds after train departure. A high-pass hamming window filter is used to obtain a mean of zero for the time history of the strain estimation error ($\delta\boldsymbol{\varepsilon}_p$). Figure 20 shows the error estimated for each zone defined over the time history of a train ride. The prediction error at each zone is assumed to follow a Gaussian distribution

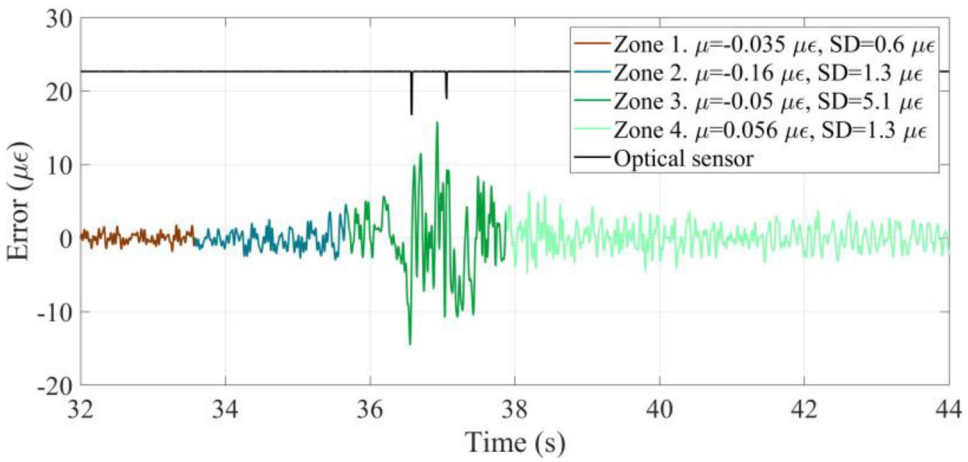

Fig. 20 Strain estimation error ($\delta\boldsymbol{\varepsilon}_p$) time history for MUME predictions

with zero mean and a different standard deviation obtained using the residuals as stated in Eq. (3).

A larger standard deviation is calculated during the train passage and right after the train passage (zone 3) in Fig. 20. Within this zone, the standard deviation of the error is calculated at 5.1 με. Prediction errors are provided for the estimated strain time histories in Fig. 21. Estimated strains using MUME method show to be in good agreement with measured strains and within a 95% quantile interval (i.e., ±2 error standard deviation).

4.2 Method 2: AKF

In this section, the AKF is used with a substructure of the instrumented connection for the prediction of response as proposed in previous research [36]. The updated FEM model, using Method 1, and the AKF are used to determine strains at unmeasured locations. Fig. 18 shows the prediction of normal and shear strains at the left-front of the connection. These strain history predictions are based on measurements from the left-back and right-front rosettes. The tuning of covariance matrices for the process and measurement noise is performed heuristically, based on time histories of normal and shear strains obtained from strain rosette measurements. The covariance of the process Q and measurement noise R are tunable parameters, which are configured based on the confidence that may be attributed to the precision of the model and the measurements respectively. The range of these covariances depends on the range of the state and measurement variables themselves (unless regularization is employed). This is due to the additive effect in the calculation of the prior state and innovation covariance (which participates in the calculation of the Kalman gain). More importantly, however, it is the ratio of these covariance (QR^{-1}) that largely affects the convergence of the estimates. The interested reader is referred to this work for a formal analysis on the effects of these noise sources [61].

Based on the above discussion, after tuning, the process noise standard deviation for the state is set to 10^{-11} for the response and 10^{-6} for the input part of the augmented state vector. In addition, the standard deviation of the measurement noise for the left-back location is set to $10^{-11}, 10^{-11}, 10^{-11}$ for ε_x, ε_y, and γ_{xy} respectively, and $10^{-13}, 10^{-12}, 10^{-12}$ for the right front location. Here, strain measurements are used, corresponding to low amplitudes, which further leads to low attributed covariance levels. When these numbers shift close to machine precision, thereby affecting algorithmic performance, regularization of the state and observation variables would be required. In this case, this was not necessary.

Predictions from Method 1 are included in Fig. 21 for comparison purposes. In addition, the confidence interval limits located at two standard deviations are shown as shaded areas. Strain measurements lie within the 95% interval in most of the time histories. The predicted strains follow the overall trend of normal and shear strains calculated from the measured data. Methods 1 (MUME) and 2 (AKF) result in accurate strain predictions at locations with high magnitude of strains while larger prediction errors are observed at locations with lower magnitude response where strains might be corrupted by measurement noise. Given that the input loads are not measured in either method and

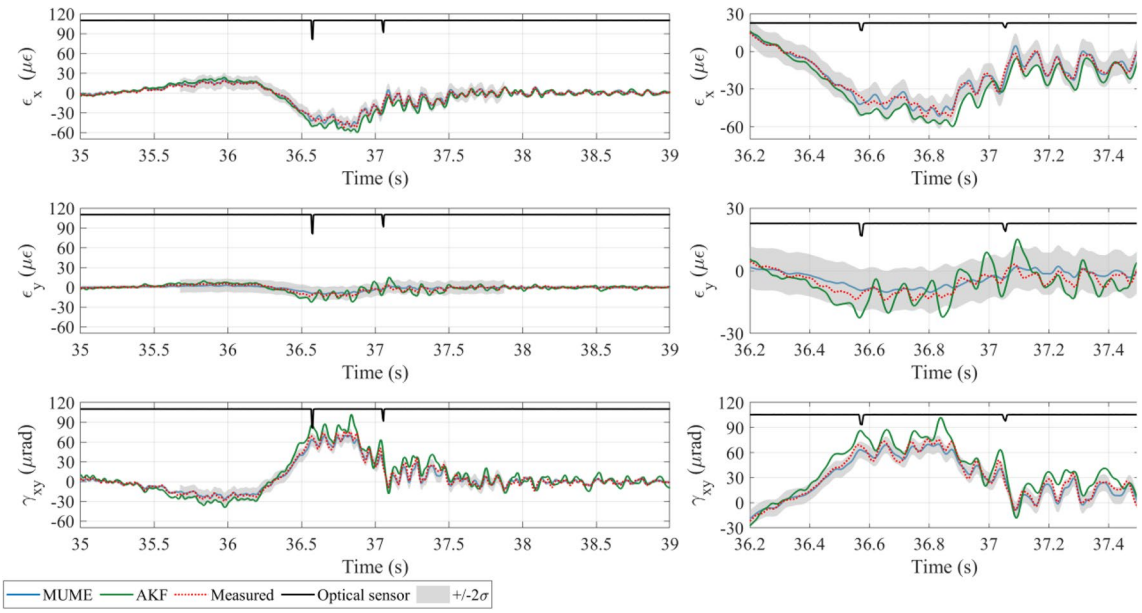

Fig. 21 Method 1 (MUME) and Method 2 (AKF) strain predictions for comparison with measured strains at the left-front location

that a heuristic approach is used for the estimation of noise covariance values when implementing the AKF, the estimated strain histories are considered to be in sufficiently good agreement with the measured strains at this location using both methods.

There are advantages and disadvantages when using the MUME method or the AKF method in a substructure. When implementing model-based predictions and model updating, the reliability of strain predictions is highly dependable to the completeness and accuracy of updated FEM and the available set of measurements. Therefore, prior to implementing MUME, a close examination of the measured data and the initial model is recommended. On the other hand, the AKF incorporates modeling and measurement uncertainties in the algorithm. However, tuning of covariance matrices for the process and measurement noise can be a time-consuming process since it is performed heuristically. The AKF does not provide a realistic prediction of error (covariance) for the estimated strain time histories, since the state covariance tends to quickly converge to a value which limit is defined by the selected tuning variances. These latter noise covariance values, i.e., the state and measurement noise covariance, is not typically corresponding to the values of the true system. Lastly, it should be noted that the implementation of the AKF requires the additional assumption of an evolution equation for the unknown input (here a random walk), which may act at the expense of accuracy, when not representative of the actual input dynamics.

4.3 Method 3: ME-AKF

In this proposed method, the state-space model of Method 2 is modified to include virtual measurement equations. In Method 2 measurements from the left-back and right-front side of the bracket are employed for prediction of strains at the location of left front rosette. ME-AKF scheme implements predictions obtained from ME at the left front rosette as new observations in the AKF. Process and measurement noise are modified to tune the new system. The process noise standard deviation of the state is set to 10^{-11} and 10^{-5} for the input part of the augmented state vector. In addition, the measurement noise standard deviation for the left-back location is modified to $10^{-13}, 10^{-13}, 10^{-13}$ for ε_x, ε_y, and γ_{xy} respectively, $10^{-13}, 10^{-13}, 10^{-13}$ for the right front location, and $10^{-15}, 10^{-14}, 10^{-14}$ for the left-front location, which is the virtual location. The lower noise levels of the virtual observation imply that higher levels of confidence are given to ME predictions. The addition of virtual ME-based strain predictions to this modified system provides additional information regarding nearby DOFs, forcing the filter to correct states linked to the unknown location of interest. Figure 22 shows the obtained strain time histories using ME-AKF scheme as well as MUME and AKF for comparison purpose.

Strain time history comparisons show that the implementation of additional stain observations yields predictions closer to the measured strains. Table 5 shows the RMS error for each predicted strain history. Although predictions from the previously implemented AKF resulted in relatively good overall estimates, additional information derived from ME strain predictions improves ME-AKF results. In addition, ME predictions can be especially valuable if engineering judgment is used to determine the most informative mode shapes and measurements. While predictions by MUME are comparable to ME-AKF, the execution of the AKF algorithm allows for online application at little computational cost. Both ME and AKF methods have the potential to be run in real-time, i.e., in online estimation mode. An online ME implementation involves first the calculation of the $\mathbf{\Phi}^{+}_{\varepsilon,m}$ matrices for each predicted location offline. Figure 23 shows the standard deviation derived from the covariance of the state estimate by means of the AKF algorithm. The value of the standard deviation is progressively reduced as strain predictions are estimated over time for Methods 2 and 3. However, the standard deviations of the estimated strains decrease rapidly, in less than a second to values of 10^{-7} microstrains in the ME-AKF, while the AKF converges at a much higher value. This trend is indicative of the faster convergence of the ME-AKF algorithm, yet it should be noted that these predictions for the state covariance – as aforementioned—are not yielding a realistic estimate of the uncertainty that is present within the strain estimates. A more realistic estimate is delivered by means of the proposed empirical rule introduced in Eq. (7) in the context of the MUME approach.

The robustness of strain predictions from the implementation of the ME-AKF utilizing a substructure in an in-service complex structure has been demonstrated by directly comparing measured strain time histories with predictions of classical approaches. When applying the ME-AKF method, it should be noted the potential implementation of this method to real-time estimates. Since tuning of the filter can take place in an offline preparatory phase, e.g., when instrumenting a new system, the predicted state (displacement, velocity, and acceleration) following tuning completion can be used for real-time estimations and fast decision making.

5 Discussion

This paper presents an output-only framework for strain prediction in unmeasured locations of a monitored complex structure. The case study of a connection of an in-service rollercoaster is presented for illustrating the proposed approach. Three virtual sensing approaches are utilized for the estimation of strain time histories at unmeasured locations within the connection. The first methodology is

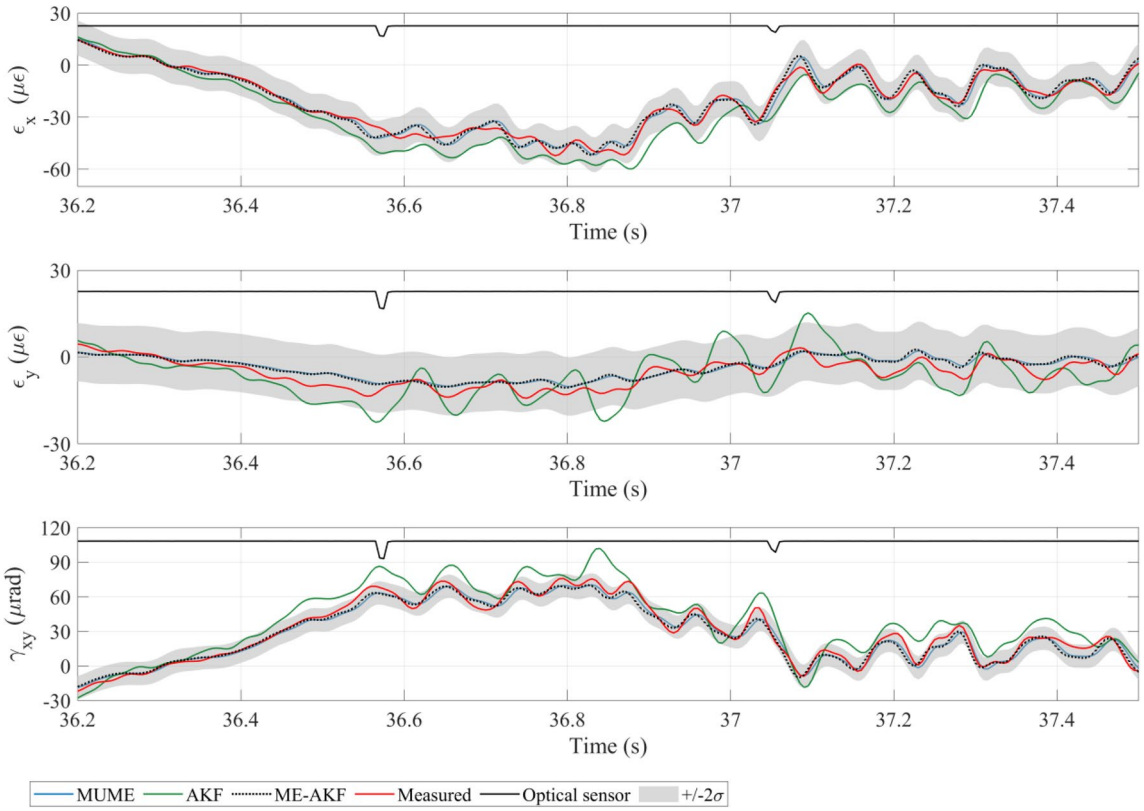

Fig. 22 Method 1 (MUME), Method 2 (AKF) and Method 3 (ME-AKF) strain predictions and comparison with measured strains at the left-front location

Table 5 RMS error strain predictions

	ε_x (με)	ε_y (με)	γ_{xy} (μrad)
MUME	1.3	1.4	2.4
AKF	3.7	2.4	6.4
ME-AKF	1.3	1.4	2.2

based on classical model updating and modal expansion (MUME) to estimate a mapping of the strain response at unmeasured locations of an instrumented connection. The second methodology employs the Augmented Kalman filter (AKF) and a model of a substructure of the instrumented connection for dynamic estimation of strain response at unmeasured locations. A comparison of these two methods allows for a cross-validation and recognition of the advantages and disadvantages in their implementation. Subsequently, a third method is proposed. The ME-AKF method makes use of predicted strain histories from ME as virtual observations in the AKF. All three methods rely on the utilization of a mechanics-based structural model. In addition, a substructuring technique is implemented to reduce computational effort in all methods. The output-only methods presented in this research employ the dynamic response from strain rosettes and require no knowledge of input forces.

A direct comparison of measured and predicted strain time histories demonstrates that the strain predictions obtained from all approaches provide reliable estimates of strain time histories during train passage. Considering (i) the low SNR at some of the sensors, and (ii) the lack of input load measurements, the estimated strain time histories provide sufficiently good agreement with the measured strains using all methods. However, the proposed ME-AKF methodology provides slightly more accurate predictions without the need for batch processing of data.

Although the accuracy of classical approaches such as the MUME scheme have been well documented and tested, this paper extends this prediction with an estimate of prediction errors which provides realistic confidence bound for strain predictions. The AKF is implemented in an in-service set-up with sparse strain-only measurements. Contrary to MUME, AKF is a Bayesian estimation scheme that allows for the consideration of modeling errors and measurement noise. However, non-optimal tuning of the process noise and measurement noise covariances can cause inaccuracies in the predicted strain histories. On the other hand, the predictions using MUME procedure

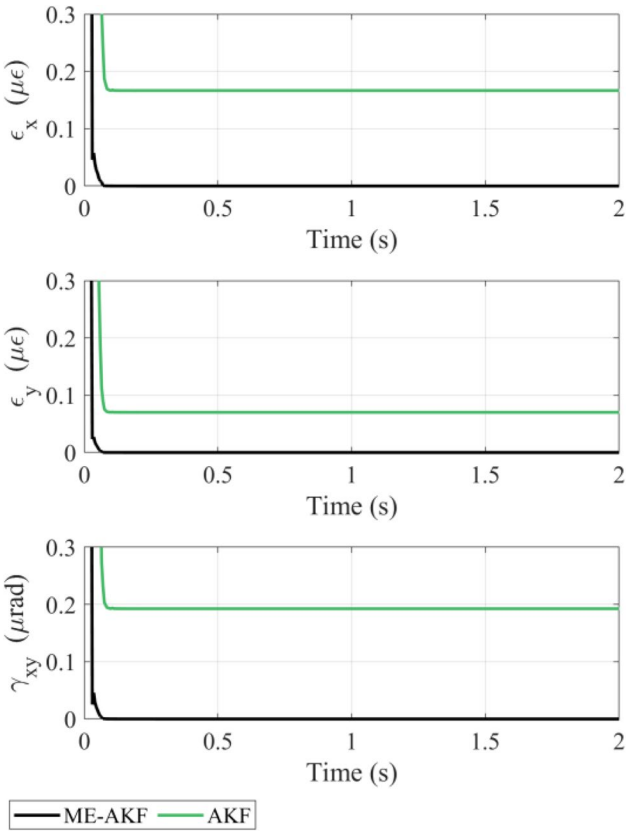

Fig. 23 Method 2 (AKF) and Method 3 (ME-AKF) Standard Deviation

are highly dependent on the quality of the model, while the AKF shows more flexibility regarding modeling errors and can still provide reasonably accurate results in the presence of large modeling errors. AKF predictions can be improved if additional observations are included in the system. Additional observations can be virtual as proposed in this study. The weight of different observations in the ME-AKF can be adjusted based on the level of confidence on different observations. For example, in this study, the virtual observations from ME are assigned lower error covariance compared to the error covariance assigned to actual sensor measurements due to the high level of confidence on the MUME results.

Tuning of the AKF filter can be a cumbersome process but it can be performed offline and in a preliminary step. Therefore, the predicted time histories following tuning completion can be used for real-time estimations and fast decision making. Automation of the tuning of the AKF's process is preferable and suggested as subject for further research. Although the effectiveness of the AKF is demonstrated using limited control locations, predictions at critical locations (e.g., weld lines) can be demonstrated in further research.

In addition, assumptions made during the modeling process, and mathematical approximations when updating the FE model can affect the predictive accuracy in the methods presented. It should be noted that in the case of AKF these assumptions do not refer only to the system itself, but also to the dynamic model describing the unknown input (random walk is considered in this study). The presence of errors due to the modeling and measurements noise in field monitoring data, is unavoidable and limits the precision of strain estimates. Nevertheless, the prediction errors are mitigated in the ME-AKF compared to the AKF results.

The proposed Method 3: ME-AKF is a versatile method offering great promise for implementation in any complex structure experiencing unknown dynamic loading such as bridges, wind turbines, transmission towers, and machinery. The applicability of the proposed methodology is demonstrated and evaluated with operational strain measurements obtained from a rollercoaster support structure.

This paper proposes practical approaches anticipated to be utilized for fatigue prognosis, stress distribution evaluation, or structural performance assessment under existing or future loading. In addition, an output-only framework comes with the added benefit of applicability during in-service conditions if instrumentation can be permanently in place.

6 Conclusions

In this study, three methods (MUME, AKF and ME-AKF) are successfully implemented and compared for estimation of strain time histories at unmeasured locations of a rollercoaster connection using sparse sensor measurements. Strain predictions from all methods closely predict the measured strain time histories at a control point. The MUME method enables the prediction of unknown strains at unknown locations making use of batch data. This method benefits from engineering judgement for improvement of strain predictions as these predictions are highly dependent on the used finite element model as well as the quality of data. Realistic confidence bounds are derived for the estimated strain time histories through an empirical approach. The accuracy of confidence bounds is verified when comparing the predicted response to the measured counterparts. The AKF method enables prediction of unknown strains at unknown locations in an online mode. The AKF method is more forgiving about possible modeling errors due to its flexibility. However, the AKF strain predictions are not as accurate as the MUME predictions. Therefore, the ME-AKF is proposed as a new scheme that improves AKF strain predictions via use of additional virtual data from ME as new observations in the AKF. This proposed method improves the predictions of the AKF and can reliably be used for real-time prediction of strains of complex connections at unmeasured locations. The

weight of the additional virtual observations compared to the sensor data can be tuned based on their relative level of confidence. All three methods have advantages for application in different settings based on the needs of the project as discussed in this paper.

Acknowledgements Data required to conduct the research presented in this paper would not have been possible without the collaboration of Mike Neuzil who provided the research team access and resources to accomplish data acquisition of the rollercoaster used in this research and also accommodating the use of LiDAR for geometric mapping. In addition, the authors would like to thank Dr. Jesse D. Sipple from BDI for helpful discussions and technical advice on setup of a wireless data acquisition system using various sensor types.

Funding The writers are grateful for the funding of this research by NSF Division of Industrial Innovation and Partnership (IIP) Grant No. IIP-1640693. PFI: AIR-TT: Real-Time Fatigue Life Prediction for Decision-making and Asset Management. Any opinions, findings, and conclusions or recommendations expressed in this research are those of the authors and do not necessarily reflect the views of the National Science Foundation.

Data availability Limited availability to strain, acceleration, and optical sensor data measured from the rollercoaster support bracket used during this research. Some data can be made available by a request to the corresponding author and upon approval from the amusement park management.

Code availability Relevant code to this research is limited. Availability can be granted by a request to the corresponding author and upon approval from the amusement park management.

Declarations

Conflicts of interest The authors have no conflict of interest to declare.

References

1. ASTM (2018) ASTM F2291–18 standard practice for design of amusement. Rides Dev 1:65
2. ASTM (2019) F770–19 Standard practice for ownership , operation , maintenance , and inspection of amusement rides and devices. www.astm.org, West Conshohocken, PA
3. AASHTO (2018) Manual for Bridge Evaluation (3rd Edition). Am Assoc State Highw Transp Off
4. ABSG Consulting Inc (2015) Offshore wind energy inspection procedure assessment
5. Kullaa J (2016) Virtual sensing of structural vibrations using dynamic substructuring. Mech Syst Signal Proc 79:203–224. https://doi.org/10.1016/j.ymssp.2016.02.045
6. Vettori S, Lorenzo E Di, Cumbo R, Musella U, Tamarozzi T, Peeter B, Chatzi E (2019) Kalman-based virtual sensing for improvement of service responses replication in environmental tests. In: IMAC XXXVIII Conference. The Society of Experimental Mechanics, Orange County, California, Houston, Texas, p #8071
7. Tarpø M, Nabuco B, Georgakis C, Brincker R (2019) The effect of operational modal analysis in strain estimation using the modal expansion. In: 8th IOMAC - International Operational Modal Analysis Conference, Proceedings. Copenhagen, pp 699–705
8. Yu H, Mohammed MA, Mohammadi ME, Moaveni B, Barbosa AR, Stavridis A, Wood RL (2017) Structural identification of an 18-story RC building in Nepal using post-earthquake ambient vibration and lidar data. Front Built Environ 3:1–15. https://doi.org/10.3389/fbuil.2017.00011
9. Iliopoulos A, Weijtjens W, Van Hemelrijck D, Devriendt C (2016) Full-Field strain prediction applied to an offshore wind turbine bt - model validation and uncertainty quantification, volume 3. In: Schoenherr T, Moaveni B, Papadimitriou C (eds) Atamturktur S. Springer, Cham, pp 349–357
10. Soman R, Ostachowicz W (2018) Kalman filter based load monitoring in beam like structures using fibre-optic strain sensors. Sensors (Basel) 19:103. https://doi.org/10.3390/s19010103
11. Eftekhar Azam S, Chatzi E, Papadimitriou C (2015) A dual Kalman filter approach for state estimation via output-only acceleration measurements. Mech Syst Signal Proc 60:866–886. https://doi.org/10.1016/j.ymssp.2015.02.001
12. Papadimitriou C, Fritzen C-P, Kraemer P, Ntotsios E (2011) Fatigue predictions in entire body of metallic structures from a limited number of vibration sensors using Kalman filtering. Struct Control Heal Monit 18:554–573. https://doi.org/10.1002/stc
13. Astroza R, Ebrahimian H, Conte JP (2017) Batch and Recursive Bayesian estimation methods for nonlinear structural system identification BT - risk and reliability analysis: theory and applicationsn Honor of ProfArmen Der Kiureghian. In: Gardoni P (ed) Armen Der Kiureghian. Springer, Cham, pp 341–364
14. Briers M, Doucet A, Maskell S (2004) Smoothing Algorithms for State-Space Models. IEEE Trans SIGNAL Process
15. Baqersad J, Bharadwaj K (2018) Strain expansion-reduction approach. Mech Syst Signal Process 101:156–167. https://doi.org/10.1016/j.ymssp.2017.08.023
16. Pingle P, Avitabile P (2011) Full field dynamic stress/strain from limited sets of measured data. Conf Proc Soc Exp Mech Ser 2:187–200. https://doi.org/10.1007/978-1-4419-9305-2_13
17. Avitabile P, Pingle P (2012) Prediction of full field dynamic strain from limited sets of measured data. Shock Vib 19:765–785. https://doi.org/10.3233/SAV-2012-0686
18. Tarpø M, Nabuco B, Georgakis C, Brincker R (2020) Expansion of experimental mode shape from operational modal analysis and virtual sensing for fatigue analysis using the modal expansion method. Int J Fatigue 130:105280. https://doi.org/10.1016/j.ijfatigue.2019.105280
19. Juang JN, Pappa RS (1985) An eigensystem realization algorithm for modal parameter identification and model reduction. J Guid Control Dyn 8:620–627. https://doi.org/10.2514/3.20031
20. James GH, Carne TG, Lauffer JP (1995) the natural excitation technique (NExT) for modal parameter extraction from operating structures. Modal Anal Int J Anal Exp Modal Anal 10:260–277
21. Moncayo H, Marulanda J, Thomson P (2010) Identification and monitoring of modal parameters in aircraft structures using the natural excitation technique (NExT) combined with the eigensystem realization algorithm (ERA). J Aerosp Eng 23:99–104. https://doi.org/10.1061/(ASCE)AS.1943-5525.0000011
22. Yingnan G, Fangyi W (2013) Research on modal parameters identification of wing structures with NExT-ERA. Appl Mech Mater 249–250:1025–1029
23. Moaveni B, Barbosa AR, Conte JP, Hemez FM (2014) Uncertainty analysis of system identification results obtained for a seven-story building slice tested on the UCSD-NEES shake table. Struct Control Heal Monit 21:466–483. https://doi.org/10.1002/stc.1577
24. Mieloszyk M, Opoka S, Ostachowicz W (2015) Frequency domain decomposition performed on the strain data obtained from the aluminium model of an offshore support structure. J Phys Conf Ser. https://doi.org/10.1088/1742-6596/628/1/012111

25. Kranjc T, Slavić J, Boltežar M (2016) A comparison of strain and classic experimental modal analysis. JVC/Journal Vib Control 22:371–381. https://doi.org/10.1177/1077546314533137
26. Peng Z, Dong K, Yin H (2019) A modal-based kalman filter approach and Osp method for structural response reconstruction. Shock Vib 2019:5475686. https://doi.org/10.1155/2019/5475686
27. Palanisamy RP, Cho S, Kim H, Sim SH (2015) Experimental validation of Kalman filter-based strain estimation in structures subjected to non-zero mean input. Smart Struct Syst 15:489–503
28. Erazo K, Sen D, Nagarajaiah S, Sun L (2019) Vibration-based structural health monitoring under changing environmental conditions using Kalman filtering. Mech Syst Signal Process 117:1–15. https://doi.org/10.1016/j.ymssp.2018.07.041
29. Simon D (2006) Optimal state estimation: kalman, h infinity, and nonlinear approaches. Wiley-Interscience
30. Azam ES, Chatzi E, Papadimitriou C, Smyth A (2017) Experimental validation of the kalman-type filters for online and real-time state and input estimation. J Vib Control 23:2494–2519. https://doi.org/10.1177/1077546315617672
31. Dertimanis V, Chatzi E, Eftekhar Azam S (2016) Papadimitriou C (2016) Output-only fatigue prediction of uncertain steel structures. Eur Work Struct Heal Monit EWSHM 2:5–8
32. Lagerblad U, Wentzel H, Kulachenko A (2018) Fatigue damage prediction based on strain field estimates using a smoothed kalman filter and sparse measurements. In: Proceedings Of ISMA2018 and USD2018. pp 2805–2818
33. Tatsis KE, Dertimanis VK, Papadimitriou C, Lourens E, Chatzi EN (2021) A general substructure-based framework for input-state estimation using limited output measurements. Mech Syst Signal Process 150:107223. https://doi.org/10.1016/j.ymssp.2020.107223
34. Noppe N, Tatsis K, Chatzi EN, Devriendt C, Weijtjens W (2018) Fatigue stress estimation of offshore wind turbine using a kalman filter in combination with accelerometers. In: PROCEEDINGS OF ISMA2018 AND USD2018. pp 4847–4856
35. Ansys® (2017) ANSYS Documentation. DeignXplorer User's Guide
36. Puerto Tchemodanova S, Tatsis K, Dertimanis V, Chatzi E (2019) Remaining fatigue life prediction of a roller coaster subjected to multiaxial nonproportional loading using limited measured strains locations (Under review). Struct Congr 4:1–11
37. Caicedo JM (2011) Practical guidelines for the natural excitation technique (NExT) and the eigensystem realization algorithm (ERA) for modal identification using ambient vibration. Exp Tech 35:52–58. https://doi.org/10.1111/j.1747-1567.2010.00643.x
38. Allemang RJ, Brown DL (1998) A unified matrix polynomial approach to modal identification. J Sound Vib 211:301–322. https://doi.org/10.1006/jsvi.1997.1321
39. Saltelli A, Tarantola S, Campolongo F, Ratto M (2002) Sensitivity analysis in practice. John Wiley and Sons Ltd
40. Cundy AL (2003) Use of response surface metamodels in damage identification of dynamic structures. Virginia Polytech Inst State Univ Master Sci Thesis
41. Qintao G, Lingmi Z (2004) Finite element model updating based on response surface methodology. Proc 22nd IMAC Dearborn,:306–309
42. Zong Z, Lin X, Niu J (2015) Finite element model validation of bridge based on structural health monitoring—Part I: Response surface-based finite element model updating. J Traffic Transp Eng (English Ed 2:258–278 . https://doi.org/https://doi.org/10.1016/j.jtte.2015.06.001
43. Kianifar MR, Campean F (2020) Performance evaluation of metamodelling methods for engineering problems: towards a practitioner guide. Struct Multidiscip Optim 61:159–186. https://doi.org/10.1007/s00158-019-02352-1
44. Skafte A, Kristoffersen J, Vestermark J, Tygesen UT, Brincker R (2017) Experimental study of strain prediction on wave induced structures using modal decomposition and quasi static Ritz vectors. Eng Struct 136:261–276. https://doi.org/10.1016/j.engstruct.2017.01.014
45. Oppenheim AV, Schafer RW, Buck JR (1999) Discrete-time signal processing. Prentice Hall
46. Chandrupatla TR, Belegundu AD (2015) Introduction to finite elements in engineering, 4th edn. Prentice Hall
47. Lourens E, Reynders E, De RG, Degrande G, Lombaert G (2012) An augmented Kalman filter for force identification in structural dynamics. Mech Syst Signal Process 27:446–460. https://doi.org/10.1016/j.ymssp.2011.09.025
48. Maes K, Lourens E, Van Nimmen K, Reynders E, De Roeck G, Lombaert G (2015) Design of sensor networks for instantaneous inversion of modally reduced order models in structural dynamics. Mech Syst Signal Process 52–53:628–644. https://doi.org/10.1016/j.ymssp.2014.07.018
49. Butler JL, Sherman CH (2016) Transducers and Arrays for Underwater Sound
50. FARO Technologies Inc (2016) FARO Focus 3D X 330 HDR The Imaging Laser Scanner for Extended Ranges
51. FARO Technologies Inc (2010) FaroArm® Platinum
52. Horváth P (2018) Efficiency and accuracy investigation of the Craig-Bampton method through continuum vibration tests. AIP Conf Proc. https://doi.org/10.1063/1.5019121
53. De KD, Rixen DJ, Voormeeren SN (2008) General framework for dynamic substructuring: history, review and classification of techniques. AIAA J 46:1169–1181. https://doi.org/10.2514/1.33274
54. Bampton M, Craig R (1968) Coupling of substructures for dynamic analyses. AIAA J 6:1313–1319
55. Papadimitriou C, Papadioti DC (2013) Component mode synthesis techniques for finite element model updating. Comput Struct 126:15–28. https://doi.org/10.1016/j.compstruc.2012.10.018
56. Zhu D, Dong X, Wang Y (2016) Substructure stiffness and mass updating through minimization of modal dynamic residuals. J Eng Mech 142:04016013. https://doi.org/10.1061/(ASCE)EM.1943-7889.0001063
57. Tatsis K, Dertimanis V, Abdallah I, Chatzi E (2017) A substructure approach for fatigue assessment on wind turbine support structures using output-only measurements. Proc Eng 199:1044–1049. https://doi.org/10.1016/j.proeng.2017.09.285
58. Chang M, Pakzad SN (2013) Modified natural excitation technique for stochastic modal identification. J Struct Eng (United States) 139:1753–1762. https://doi.org/10.1061/(ASCE)ST.1943-541X.0000559
59. He X, Moaveni B, Conte JP, Elgamal A, Masri SF (2009) System identification of alfred zampa memorial bridge using dynamic field test data. J Struct Eng 135:54–66. https://doi.org/10.1061/(ASCE)0733-9445(2009)135:1(54)
60. Yam LH, Leung TP, Li DB, Xue KZ (1996) Theoretical and experimental study of modal strain analysis. J Sound Vib 191:251–260. https://doi.org/10.1006/jsvi.1996.0119
61. Rhudy MB, Gu Y (2013) Online stochastic convergence analysis of the Kalman filter. Int J Stoch Anal. https://doi.org/10.1155/2013/240295